Influence of a Liquid Electrolyte on Electronic and Ionic Transfers in a LiNi 0.5 Mn 0.3 Co 0.2 O 2 /Poly(vinylidene Fluoride- co -hexafluoropropylene)-Based Composite Material

Anshuman Agrawal, Olivier Dubrunfaut, Loïc Assaud, Sylvain Franger, Bernard Lestriez, Jean-Claude Badot

Influence of a Liquid Electrolyte on Electronic and Ionic Transfers in a $LiNi_{0.5}Mn_{0.3}Co_{0.2}O_2$ / Poly(vinylidene fluoride-co-hexafluoropropylene) based Composite Material

*Anshuman Agrawal,[1,2,3,4] Olivier Dubrunfaut,[1] Loïc Assaud,[2] Sylvain Franger,[2] Bernard Lestriez,[3] and Jean-Claude Badot [4,5]**

[1] GeePs Group of electrical engineering - Paris, UMR CNRS 8507, CentraleSupélec, Sorbonne Universités, Université Paris-Saclay, 11 rue Joliot-Curie, 91192 Gif-sur-Yvette, France
[2] ICMMO ERIEE, Université Paris-Saclay, UMR CNRS 8182, Rue du Doyen Georges Poitou, 91400 Orsay, France
[3] Institut des Matériaux Jean Rouxel, UMR CNRS 6502, Université de Nantes, 2 rue de la Houssinière, BP32229, 44322 Nantes, France
[4] Chimie ParisTech, PSL Research University, CNRS, Institut de Recherche de Chimie Paris, 75005 Paris, France
[5] Réseau sur le Stockage Electrochimique de l'Energie (RS2E), FR CNRS 3459, France

*Corresponding Author jc.badot@chimie-paristech.fr

Abstract

The permittivity and conductivity of a porous composite consisting of a mixture of a lithium ion battery electrode material, $LiNi_{0.5}Mn_{0.3}Co_{0.2}O_2$ (NMC532), and a polymeric binder, Poly(vinylidene fluoride-co-hexafluoropropylene) (PVdF-HFP), were simultaneously measured by broadband dielectric spectroscopy (BDS). The composite was either dry or wetted with a conventional battery electrolyte (LP30, $LiPF_6$ in EC:DMC) or a mixture of electrolytic solvents (EC:DMC). The experimental results show that the electronic conductivity of NMC532 was much higher than that obtained with $LiNi_{0.33}Mn_{0.33}Co_{0.33}O_2$ (NMC333). In addition, a strong influence of liquids was evidenced. Dipolar species (in particular EC dipoles), and ions (in particular PF_6^- in LP30) considerably increased the surface conductivity of NMC532 clusters, leading to a facilitated electronic transfer from one cluster to another. The effective ionic conductivity was measured and compared to the ionic conductivity of the electrolyte to express the tortuosity factor of this composite electrode.

1. INTRODUCTION

Lithium-ion (LiB) batteries are widely used today to store energy for many different applications such as electric vehicle, electronic portable device or energy harvesting. It remains necessary to improve their performances, in particular for electric vehicles, for which it is necessary to extend the autonomy and reduce the charging time. LiB's electrodes consist of a complex hierarchical composite materials mixture, containing an active material (AM) in powder form mixed together with an electronically conductive carbon black powder and a polymeric binder. The performances of LiBs are significantly dependent on the electron and ion transport properties within the composite electrodes, which crucially depend on their nano-, meso- and macrostructure, exhibiting several interfaces that connect the different material compounds to each other, and transport paths of varying lengths.[1]

Conventional electrochemical impedance spectroscopy (EIS) from 10^{-3} to 10^{6} Hz and four-probe direct-current (dc) techniques do not allow easy measurements and understanding of electronic transfers in electrode materials for lithium batteries. The former allows to determine the macroscopic interfacial charge transfer and the macroscopic ionic diffusion in the electrodes during electrochemical cycling process, whereas the latter provides a precise measurement of the dc conductivity which is the response of the long-range electronic transport at the macroscopic scale of the material. Indeed, the existence of numerous interfaces within the electrodes constitutes barriers limiting the electronic flux which leads to a lack of information regarding the mechanistic approach of the electronic conduction. It is thus necessary to use a technique which can at once detect slower ionic motions and faster electronic motions respectively at lowest and highest frequency ranges. The broadband dielectric spectroscopy (BDS) is a unique technique for this purpose, allowing to measure complex permittivity and conductivity over a wide frequency range from 10 Hz to 18 GHz with respect to temperature variation.[2,3,4,5,6,7] Note that if EIS and BDS can bring some

identical information, at a certain point, they are mostly complementary (and not similar) since: the setups are different (1 electrode in BDS vs 2 or 3 electrodes in EIS), the signals are different (EM wave in BDS vs AC in EIS), and the subsequent equations to interpret the date are different (Maxwell eq. in BDS vs Buttler-Volmer eq. in EIS). Indeed, data that can be fitted by equivalent electrical circuits in EIS, because of the electrochemical processes (through charge transfer thanks to a second counter electrode), is irrelevant in BDS since polarizations are studied (both at outer interface of the grains, inside the solvent layer, and at inner interface inside the solid particles, behaving as a semiconductor), through the appearance/changes of space charges. Thereafter, no equivalent circuit will be able to express the exact behavior of the material, since at high frequencies it is not possible to discriminate between electrons and ions participating in an energy storage/dissipation phenomenon, as it is the case in EIS where capacitive double layer charge is decorrelated from faradaic current through the well-known R//C Randles equivalent electrical scheme. Moreover, the relationship between complex conductivity $\sigma(\omega)$ and relative permittivity $\varepsilon(\omega)$ is given by the following equation:

$$\sigma(\omega) = \rho(\omega)^{-1} = i\omega\varepsilon_0\varepsilon(\omega) \quad (1)$$

where $\rho(\omega)$ is the complex resistivity and $\varepsilon_0 = 8.84\times10^{-12}$ F.m^{-1} the vacuum permittivity. It is precisely this wide frequency range that allows to study different dispersed components in a heterogeneous mixture, which electrically polarize at different rates. This is related to both conductivity and size scale of the mixture component under consideration. As an example, considering the same active material, a particle will be studied at higher frequencies than the corresponding agglomerate (or cluster) of particles, as a material polarizes faster at smaller scales. The electrical properties of composite electrodes are difficult to understand due to their complex hierarchical nature (existence of agglomerates of active material and carbon black) and thus to the presence of various interfaces at the different scales of the electrode: current

collector/electrode contact, particle boundaries within active material agglomerate, junctions between carbon black agglomerates separated by insulating binder layers, and carbon black/active material contacts. The different interfaces thus produce charge accumulations at agglomerate and particle junctions or boundaries. As a result, electric polarizations at the different scales of the composite electrode (Fig. 1a) take place. Corresponding relaxation frequency is even larger as the mobility of the charge carriers (e.g. electrons) involved is higher and the size of the system is smaller. Previous BDS studies have distinguished the different types of interfaces inducing multiscale electric polarizations and conductivities, notably in $LiNi_{0.33}Mn_{0.33}Co_{0.33}O_2$ (called NMC333) active material. In particular, strong interactions between ions (Li^+, PF_6^-) of the electrolyte and electrons involved in NMC333 and carbon black (CB) conductivities have been evidenced. These interactions depend on the type of conduction of the active material (i.e. p or n type) and on the nature of the species (i.e. dipoles or ions) adsorbed on its surface.

The $LiNi_{0.5}Mn_{0.3}Co_{0.2}O_2$ (hereafter denoted NMC532) active material is increasingly replacing NMC333 in today's LiB as a consequence of superior performance.[8] The present study is focusing on NMC532, intending to better understand the electrochemical properties of NMC532-based LiB electrodes.[9]

Exhaustive characterization of the multiscale electronic transport in NMC532 is performed without adding the CB conducting additive in order to: (i) provide a comparison with NMC333; and (ii) reveal the interactions of the electrolyte with NMC532. A systematic approach is followed, studying the samples at different temperatures, starting with a study of NMC532 in the dry state, then wetted with ethylene carbonate (EC) – dimethyl carbonate (DMC) solvent and finally soaked with LP30 electrolyte ($LiPF_6$ 1 molar in 1:1 v:v EC:DMC). The active material was compounded with the poly(vinylidene fluoride-co-

hexafluoropropylene) (PVdF-HFP) binder, hereafter abbreviated to PVdF, to form a pellet. The amount of PVdF and the porosity of the pellet are also parameters of the study.

2. EXPERIMENTAL SECTION

2.1. Materials

The NMC powder under study was an EV battery grade material.[9,10,11] NMC/PVdF mixtures were prepared according to protocols described elsewhere.[5] Cylindrical samples of 7-mm diameter were obtained by compacting the NMC/PVdF using a pelletizer (Ets Canaple) at about 750 MPa.

SEM images and EDX analysis of the NMC powder were performed using a Zeiss Supra 55 variable pressure scanning electron microscope with field emission gun (SEM-FEG), equipped with energy dissipative X-ray detector for chemical microanalysis. X-ray diffraction patterns were measured in a PANalytical XPert Pro diffractometer using a Cu-Kα (λ=1.5408 Å) source operating at 40 kV and 30 mA. The patterns were acquired in a θ-2θ configuration with a 2θ range of 10-80° with a step size of 0.017 °.s^{-1}. Complementary characterizations of the NMC powder by EBSD (Electron Backscatter Diffraction), X-Ray and FIB/SEM tomography techniques can be found elsewhere.[10]

2.2. Broadband dielectric spectroscopy

BDS measurements were carried out by placing a sample at the discontinuity of a coaxial waveguide. Agilent 4294 (40 to 1.1×10^8 Hz) and E8364B (10^6 to 1.8×10^{10} Hz) impedance and network analysers respectively were used to obtain the admittance over multiple frequency bands, with a frequency overlap ranging between 10^6 and 1.1×10^8 Hz that verifies the measurements correspondence [1-6]. The cylindrical sample filled the gap between a short-circuit and the coaxial waveguide. The sample exhibited the same diameter (i.e. 7 mm) than the outer-conductor of the coaxial waveguide and a thickness of about 400 μm. Metallic

contacts were made by gold sputtering on both front and backsides of the sample in order to provide sufficient electrical contacts. Facing the inner conductor of the coaxial cell, the gold film in the center of the sample surface had the same diameter (i.e. 3 mm) than the inner conductor. Facing the short-circuit, the gold film covered the entire surface of the sample. After an accurate calibration with analysers, homemade analytical resolution of the mode matching method was used to derive complex permittivity $\varepsilon(\omega) = \varepsilon'(\omega) - i\,\varepsilon''(\omega)$ and conductivity $\varepsilon(\omega) = \varepsilon'(\omega) - i\,\varepsilon''(\omega)$ of the sample. Dielectric spectra were made up of 400 measuring points with a relative accuracy at most of the order of 5%. The experimental devices are fully described in previous papers.[3,5,7] Permittivity and conductivity of the samples were measured in the temperature range 200 - 300 K under dry N_2.

3. RESULTS AND DISCUSSION

3.1. Structure and microstructure

Figure 1a shows the intimate relationship between the frequency range and the size of the objects of interest. Scanning electron micrographs displayed on Figure 1b shows the typical $LiNi_{0.5}Mn_{0.3}Co_{0.2}O_2$ compound morphology. The overall diameter of near spherical NMC clusters (Figure 1b) is about 5 μm and the size distribution can be appreciated by the d_{10}-d_{90} interval equal to 3.2 to 14.5 µm. Each cluster consists of an agglomeration of primary particles of NMC (Figure 1) exhibiting a mean diameter of about 260 nm and the size distribution can be appreciated by the d_{10}-d_{90} interval equal to 150 to 450 nm.[10] One can observe on the SEM micrographs that several interfaces are present at the different scales: cluster-cluster, cluster-particle, particle-particle with the additional contribution of the microstructure scale (interatomic distances). We assume that these interfaces strongly contribute to limitations in terms of both the effective surface and bulk electronic conductivities of the NMC compound as suggested in a previous study.[12] It has to be noted

that calendered electrodes were also studied, exhibiting fracturing of some of the NMC clusters due to the applied tonnage.[10]

A complementary chemical microanalysis of the powder performed by energy dissipative X-ray spectroscopy (EDS) (Figure 1c) allowed to determine the stoichiometry of the materials. The composition of the sample is in perfect agreement with the expectations, each TM being in the right atomic percent: Ni (49.77 %), Mn (28.75 %) and Co (21.48 %). Empirically, one would expect there are 80% Ni^{2+}, 20% Ni^{3+} in stoichiometric pristine NMC532.

Structural investigations of the $LiNi_{0.5}Mn_{0.3}Co_{0.2}O_2$ compound have been performed by X-ray diffraction (Figure 1d). The powder contains only one crystalline phase which matches the layered α-$NaFeO_2$ type of trigonal crystal structure (space group of $R\bar{3}m$, Figure 1e). [12] The $R\bar{3}m$ phase can be categorized as hexagonal according to the crystal family, trigonal according to the crystal system, and rhombohedral according to the lattice system. The composition is a recurring succession of a transition-metal layer at the base, followed by an oxygen fragment, a lithium layer and, again a transition-metal layer. The transition metal atoms that are correlated with the 001 plane are distributed in a hexagonal pattern (Figure 1e) where all the transition metal present in the structure are having the same probability to occupy any atomic site. [13] One can distinguish clearly the two diffraction pairs (006)/(012) and (018)/(110) that are indicating a highly crystalline layer structure. NMC clusters are however polycrystalline, as the layers orientation within each particle differs from their neighbours.[10]

3.2. Influence of PVdF on electric properties of $LiNi_{0.5}Mn_{0.3}Co_{0.2}O_2$

The addition of PVdF is necessary so that the samples to be studied are compactable in the form of pellets (see Experimental Section). Firstly, the measurements were performed by comparing two samples with different volume contents of PVdF. The former (hereafter

148 denoted N0) had 63% NMC532, 3% PVdF and 34% porosity. The second (hereafter called
149 N0b) had mean values of about 68% NMC532, 5.6% PVdF and 26.4% porosity. Note that the
150 compositions are indicated in volume percentage. N0b which has more PVdF will be fully
151 studied because it does not disintegrate when soaked with liquids (EC:DMC in 1:1 v:v and
152 LP30). Fig.2 compares the real parts of conductivity (σ′) and permittivity (ε′) spectra of N0
153 and N0b at room temperature. The results are surprising at first sight with respect to the
154 evolution of the conductivity as a function of frequency (Fig. 2a). In fact, the conductivity of
155 N0b is lower than that of N0 below 10^6 Hz and becomes higher above 10^6 Hz (Fig. 2a).
156 Below 10^6 Hz, the insulating PVdF has a major influence on the electrical properties of N0b,
157 despite a higher NMC content (68% instead of 63%). Above 10^6 Hz, the influence of NMC
158 content on the conductivity is physically more consistent. Nyquist plots of complex
159 permittivity (ε" vs. ε'), resistivity (ρ" vs. ρ') and conductivity (σ" vs. σ') are highly suitable
160 to evidence the different relaxations by means of a decomposition procedure which is
161 recorded using a homemade software. Indeed, it has been previously shown that the frequency
162 dependent permittivity of a conducting material is generally given by the following equation:

163 $$\varepsilon(\omega) = \varepsilon_{hf} + \left[\sum_j \frac{\Delta\varepsilon_j}{\left[1+(i\omega\tau_j)^{1-\alpha_j}\right]^{\beta_j}}\right] + A(i\omega)^{s-1} + \frac{\sigma_{dc}}{i\omega\varepsilon_0} \quad (2)$$

164 The term in brackets corresponds to the sum of the empirical relaxation functions (i.e.
165 Havriliak-Negami (HN) functions) because electric polarizations at different scales are
166 additive due to their vector character. In equation (2), $\omega = 2\pi\nu$ is the angular frequency in
167 rad.s^{-1} (ν being the frequency expressed in Hz). α_j ($0 \leq \alpha_j \leq 1$) and β_j ($0 \leq \beta_j \leq 1$) are fitting
168 parameters, τ_j a mean relaxation time, $\Delta\varepsilon_j$ the dielectric strength, σ_{dc} the sample dc-
169 conductivity, ε_{hf} the sample residual (or higher frequency) permittivity and s ($0 \leq s \leq 1$) an
170 empirical parameter. The relaxation functions that fit most experimental spectra are Debye (α_j
171 = 0, β_j = 1) and Cole-Cole ($\alpha_j \neq 0$, β_j = 1) functions whose Nyquist representations display

arcs of circle centered on the real axis for the first one and below this axis for the second one. The term $A(i\omega)^{s-1}$ ($0 \leq s \leq 1$), whose the contribution occurs in the low-frequency range it is due to a more or less disorderly conductive network (at macroscopic scale). It can be also due to distributions of contact resistances and capacitance between metallization and the sample. The Nyquist plot of such behavior is a straight line whose angle $\theta = (1-s)\pi/2$ with the ε'-axis is smaller as the parameter s is higher: the straight line is vertical for $s = 0$ and merged with the sample dc-conductivity contribution $\sigma_{dc}/i\omega\varepsilon_0$. The decomposition of the dielectric spectra into several contributions (DC conductivity and relaxations) is carried out by successive subtractions of the contributions starting from the lowest frequencies to the highest ones. For the sake of clarity, the dielectric spectra of N0 are fully analyzed in Supporting Information S1 (Fig. S11 and S12). The entire Nyquist plot of N0b at room temperature (Fig. 3a left) shows that the low-frequency part of the spectrum is well fitted by a quasi-vertical straight line (P1 contribution) corresponding to the sample dc-conductivity $\sigma_{dc}/i\omega\varepsilon_0$ contribution, the term $A(i\omega)^{s-1}$ being negligible. After subtracting the P1 contribution, a dielectric relaxation (P2b contribution) is found to be well fitted by a Cole-Cole (CC) function with frequency $\nu_{2b} = 2\times10^4$ Hz (i.e. $\tau_{2b} \approx 8$ μs), $\alpha_{2b} = 0.33$ and $\Delta\varepsilon_{2b} = 307$ (see Table 1). Both following P2 and P3 contributions are obtained after subtracting those of P2b and P2, respectively. The second P2 contribution is well fitted by a CC relaxation function with frequency $\nu_2 = 5\times10^5$ Hz (i.e. $\tau_2 \approx 0.32$ μs), $\alpha_2 = 0.21$ and $\Delta\varepsilon_2 = 60$ (Table 1). The third contribution P3 is also fitted by a CC relaxation function with frequency $\nu_3 = 7\times10^7$ Hz (i.e. $\tau_{2b} \approx 2.3$ ns), $\alpha_3 = 0.29$ and $\Delta\varepsilon_3 = 110$ (see Table 1). Table 1 compares the dielectric relaxations of the two compounds N0 and N0b (Supporting Information S1, Fig. S11). P2 is a space-charge relaxation occurring at largest scale of the sample and is due to the interface between the sample and gold metallization in the contact with the coaxial cell surface. The lowest frequency relaxation P2b is non-existent for N0. This shows that P2b is due to the existence of another type of interface

for which PVdF lies between gold and NMC, thus making it more difficult the electronic transfer. Hence, P2b is a space-charge relaxation over the thickness of PVdF/NMC assembly (i.e. sample thickness ~ 400 μm). P2 and P3 relaxations are each common to both samples owing to their respective frequency ranges (Table 1). At the other extremity of the dielectric spectrum, the relaxation P4 having the highest frequency remained undetected for N0b although it was highlighted for N0. This may be due to its relatively smaller intensity $\Delta\varepsilon_4$ compared to its lower frequency counterpart P3 which is two times larger than that of N0 (Table 1), thus making it more difficult to distinguish. P2, P3 and P4 are thus space-charge relaxations associated to the following scale levels of NMC532 (Fig. 1a): the first one being at a macroscopic scale (NMC sample thickness ~ 400 μm), the second at an intermediary scale (cluster size ~ 5 μm) and the third at the smallest scale (particle size ~ 260 nm). The relaxation frequencies of P3 (cluster polarization), which are observed whatever the temperature, follow an Arrhenius law

$$\nu_3 = \nu_{03}\exp\left(-\frac{E_3}{kT}\right) \quad (3)$$

with activation energy E_3 = 0.20 eV and prefactor $\nu_{03} = 2\times10^{11}$ Hz (Fig. 3b). T and k ≈ 1.38×10^{-23} $J.K^{-1}$ are the temperature and the Boltzmann constant, respectively. However, dielectric strength $\Delta\varepsilon_3$ of P3 for N0b (i.e. $\Delta\varepsilon_3 \approx 110$) is almost twice as intense as that for N0 (i.e. $\Delta\varepsilon_3 \approx 63$) because of a higher NMC content in N0b. The P4 relaxation (particle polarization) is well fitted by a CC-function with a relaxation frequency $\nu_4 = 6.4\times10^9$ Hz, a parameter α_4 = 0.08 and a dielectric strength $\Delta\varepsilon_4$ = 1.1 at room temperature (Supporting Information S1, Table 1 and Fig. S11). The relaxation frequency ν_4 follows an Arrhenius law

$$\nu_4 = \nu_{04}\exp\left(-\frac{E_4}{kT}\right) \quad (4)$$

with an activation energy E_4 ≈ 0.09 eV and a pre-factor $\nu_{04} \approx 2\times10^{11}$ Hz. Experimental data of NMC 532 and NMC333 show they have almost the same frequency pre-factors ν_{03} and ν_{04} of

cluster and particle polarizations because they are in a narrow interval from 2×10^{11} to 3.3×10^{11} Hz (Table 1). ν_{03} and ν_{04} could correspond to hole transfer between nearest neighbors Ni^{3+} and Ni^{2+} whose distance is similar in NMC532 and NMC333. The residence time τ_0 between Ni^{3+} and Ni^{2+} ions, which equals to $(2\pi\nu_{03})^{-1}$ and $(2\pi\nu_{04})^{-1}$, would be of the order of 0.5 to 0.8 ps. Note that all the (electronic) space-charge are the consequence of a depletion layer at the surface of the NMC particles.

The whole Nyquist plot of resistivity (i.e. ρ" vs. ρ') of N0b at 294 K is shown in Figure 3c. The two circular arcs show that the complex resistivity ρ(ω) of N0b is here the sum of two relaxation functions:

$$\rho(\omega) = \rho_c + \frac{\rho_s - \rho_c}{1+(i\omega\tau_2)^{1-\alpha_2}} + \frac{\rho_{sb} - \rho_s}{1+(i\omega\tau_1)^{1-\alpha_1}} \quad (5)$$

where ρ_c is the NMC cluster resistivity, ρ_s the sample (pellet) resistivity, ρ_{sb} the resistivity including the gold/sample interface. τ_1 and τ_2 are characteristic times of low and high frequency relaxations, respectively. Then $\Delta\rho_1 = (\rho_{sb} - \rho_s)$ corresponds to the resistance of the gold/sample interface and $\Delta\rho_2 = (\rho_s - \rho_c)$ to the cluster boundary resistance (Fig. 3d). Note that $\Delta\rho_1$ which does not exist for N0 is mainly due to the resistance of the set gold/PVdF/sample. However, the particle resistivity ρ_p was only highlighted for N0 by extrapolation of Nyquist spectra at highest frequencies (Fig. S12). On the contrary ρ_p is undefined for N0b because of its lower value (see Table 1). Room temperature conductivity values of the set gold/PVdF/sample $\sigma_{sb} = \rho_{sb}^{-1}$, the sample $\sigma_s = \rho_s^{-1}$, the cluster $\sigma_c = \rho_c^{-1}$ and the particle $\sigma_p = \rho_p^{-1}$ are summarized in Table 1. It is pointed out that σ_c in N0b is twice higher than that in N0 because of a higher NMC content in N0b. Fig. 3e and S13 show that sample (σ_{sb}, σ_s), cluster (σ_{CL}) and particle (σ_p) conductivities in N0b and N0 follow Arrhenius laws given by the following equation

$$\sigma_n = \sigma_{0n}\exp\left(-\frac{E_n}{kT}\right) \quad (6)$$

with n = sb, s, c and p. The activation energy values of conductivities are in the range from 0.23 to 0.27 eV (Fig. 2c), with the exception of that of the particle equal to 0.10 eV (Table 1 and Fig S13). At this point, it is fundamental to compare the conductivities of the two compounds NMC532 and NMC333 (Table 1). Previous study of density of states (DOS) of NMC333 and NMC532 has shown among other that the top of valence band is near of Fermi energy E_F. [14] The activation energy $E_p = E_F - E_V$ of particle conductivity is thus the difference between the Fermi energy and the energy E_v (i.e. top of the valence band). NMC333) and NMC532 are p-type semiconductors in which the presence of Ni^{3+} enables hole conduction on Ni 3b sites in a 2D triangular lattice. Interatomic conductivity σ_0 of NMC532 occurring between nearest neighbors Ni is undefined owing to its high value. In NMC333, the temperature independent interatomic conductivity, $\sigma_0 \approx 20$ $S.m^{-1}$, was previously shown to correspond exactly to the particle conductivity prefactor (Table 1). **Erreur ! Signet non défini.** Hence, the calculated interatomic conductivity of NMC532 (i.e. for N0) would be of about 5126 $S.m^{-1}$, thus more than one hundred times higher than that of NMC333. But, the change in Ni molar content (i.e. from 0.33 to 0.50) cannot explain such a difference in the particle conductivity of the two compounds. Transition metals atoms (Ni, Mn and Co) are randomly located on 3b sites forming a 2D triangular lattice in planes parallel to those of Li ions (3a sites) and oxygens (3c sites) (Fig. 1e). The nickel atoms each have a coordination number z = 6 in such a lattice. However, Ni atoms must be distributed so that there are enough conduction paths to ensure electronic (holes) transfers. This last condition is fulfilled because a percolation of Ni atoms network could occur above a threshold $x_c \approx 2/z$ as defined by effective medium approximation (EMA) for bond percolation. [15,16] The percolation threshold would correspond to Nickel molar content $x_c \approx 1/3$, which confirms the much higher electronic conductivity of NMC532.

The conductivity of the spherical NMC clusters are three dimensional although that of particles (as platelets) is two-dimensional. As the particles are randomly oriented in the clusters, the conduction paths are disturbed between neighboring particles. The hole transfers are thus hindered from one particle to the other. Hence, the particle boundary barriers, i.e. ($E_c - E_p$) ≈ 0.13 eV, are higher than that between two spheroidal isotropic clusters, i.e. ($E_S - E_{CL}$) ≈ 0.02 - 0.05 eV (Table 1). The difference in conductivity between the sample and the clusters (σ_c/σ_p = 263 and 357 in NMC532 and NMC333, respectively) could be mainly explained by inter-cluster contact surface smaller than their total area.

The much higher conductivity of the particles in NMC532 compared to NMC333 has an important practical influence. Indeed, for the NMC333 to work well in an electrode, it must be made up with a higher carbon black (CB) content than for the NMC532. In the latter case, it is not necessary to adjust the CB content above the percolation threshold to achieve a suitable electronic conductivity. The addition of CB would be only required to create conductive bridges between clusters. [9,11,]

3.3. Influence of the solvent and the electrolyte on conductivity and permittivity spectra.

Fig. 4a and 4b shows real parts of conductivity (σ') and permittivity (ε') spectra of the three compounds at room temperature: dry NMC (N0b), NMC (N0b) filled with EC:DMC solvent (hereafter called N0bS) and with LP30 electrolyte (hereafter called N0bE). Conductivities rise by about two to four orders of magnitude, while real parts of permittivity drop by about the same amount on the whole frequency range. Below 10^7 Hz, there is a strong increase of the conductivity, when the porous sample is filled with EC:DMC and LP30 liquids (Fig. 4a). The conductivity rise is more important for N0bE because of the presence of the ions (Li^+, PF_6^-). Above 10^8 Hz, conductivities of N0bS and N0bE are similar and are a half order of magnitude higher than the conductivity of N0b. Histograms of Fig. 4c compare conductivities of the three different samples N0b, N0bS and N0bE at both ends of the spectrum 10^2 and 10^{10} Hz

and at room temperature. At the lowest frequency, the sample conductivity is two times higher with EC:DMC but almost two order of magnitude higher with LP30. The conductivity at 10^{10} Hz is about three times higher when the sample is soaked with EC:DMC solvent or LP30 electrolyte (Fig. 4c). This increase could be the result of the occurrence of dielectric losses due to rotation of polar molecules in solvent. Permittivity at 100 Hz is two to three orders of magnitude higher when the sample is filled by EC:DMC and LP30, respectively (Fig. 4d). Furthermore, Figures S21 and S22 show the influence of the temperature on the frequency dependence of the real parts of the conductivity and permittivity. In the case of N0bS, we can see a marked drop in dielectric values at the crystallization temperature of the solvent EC:DMC, between 280 and 276 K. For N0bE, a significant decrease is also observed at the crystallization temperature of the electrolyte, between 233 and 223 K. This will be confirmed after a thorough analysis of the spectra at different temperatures. The dielectric spectra (Fig. 4a-b and Fig. S21-S22) have several bumps due to some dielectric relaxations and conductivity, as detailed below. Moreover, when a liquid (EC:DMC or LP30) is introduced into the pore network, other types of interfaces are then created between the liquid and the different components of the electrode involving some modifications of the dielectric parameters described in Equation (2). In the following, the spectra are decomposed into several relaxations in order to reveal solvent dipoles - NMC interactions on the one hand and the ions - NMC interactions on the other hand.

3.4. Sample soaked by EC:DMC.

In this part, only the interactions of solvent dipoles with NMC532 (N0bS sample) are studied. As EC dipole moment value (i.e. 4.9 D) is greater than the dipole moment of DMC (i.e. 0.93 D), the influence of adsorbed EC dipoles on permittivity and electronic conductivity of NMC532 are only considered. The decomposition of Nyquist plots of N0bS permittivity (Fig. 5, 6a and 6b) shows the existence of three additional contributions compared to that of dry

sample N0b: a) two low-frequency relaxations P2bs and P2s (Fig. 5b and 5c) and one high-frequency relaxation P5 (Fig. 5f). This modification of the dielectric spectra is thus due to the presence of EC:DMC within the pore network of the sample. P2bs and P2s have the lowest relaxation frequencies $\nu_{2bs} = 6.1\times10^{1}$ Hz and $\nu_{2s} = 6.4\times10^{3}$ Hz at room temperature, respectively, and also have the largest intensities since their respective strengths are $\Delta\varepsilon_{2bs} = 15500$ and $\Delta\varepsilon_{2s} = 9000$. P2bs and P2s originate from interfacial capacities due to adsorbed EC dipoles at the PVdF/NMC interface and on the free NMC surface, respectively. At the other end of the spectrum, the high frequency relaxation P5 has a characteristic frequency $\nu_5 \approx 6\times10^{9}$ Hz and a dielectric strength $\Delta\varepsilon_5 \approx 10$ at room temperature. This relaxation is too intense to be attributed to NMC particle polarization whose strength is of the order of unity (Table 1). P5 contribution therefore corresponds to a rapid rotational movement of EC dipolar molecules whose value ν_5 is in the order of magnitude than that found in previous papers.[Erreur ! Signet non défini.,Erreur ! Signet non défini.] P2 and P3 are space-charge relaxations respectively attributed to sample (set of clusters) and cluster polarizations as for the dry compound. Their relaxation frequencies $\nu_2 = 5\times10^{5}$ Hz and $\nu_3 = 4.8\times10^{7}$ Hz at RT are near of that of the dry compound N0b (see Table 1 and Figure 6c). Activation energy $E_3 = 0.22$ eV and frequency prefactor $\nu_{03} = 3\times10^{11}$ Hz of ν_3 are quasi-similar to that of N0b (Fig. 6c). However, the dielectric strength $\Delta\varepsilon_3$ of P3 is higher since it is equal to 378 instead of 110 for the dry compound N0b (Fig. 6d). However, the dielectric strength $\Delta\varepsilon_3$ is equal to that of N0b, when the liquid is frozen and becomes an inert dielectric solid (Fig. 6d). In the liquid state, the dipolar EC molecules, which are adsorbed on the NMC surface, have thus an important role on intrinsic electrical properties of NMC (i.e. that of NMC cluster).

$\Delta\varepsilon_3$ is temperature independent above the freezing temperature (Fig. 6d), and thus corresponds to the space-charge capacitance (i.e. $\Delta\varepsilon_3 \alpha C_{sc}$) of the NMC cluster. The latter is

inversely proportional to its thickness w, i.e. $\Delta\varepsilon_3 \alpha C_s \alpha w^{-1}$ (Supporting Info S4 gives more details about the space-charge capacitance of p-type semiconductors, as is NMC).[17,18] The surface potential is modified and depends on the orientation of EC dipoles relative to NMC cluster surface. The electron rich carbonyl oxygen of EC is attracted to transition metal atom of NMC and EC dipole is therefore on average oriented towards the liquid.[19] Charge carriers (holes) are thus attracted toward the NMC cluster surface, which implies an increase of Ni^{3+} content, N_{surf} (the acceptors in eq. (S1) of Supporting Info S4), in the space-charge layer. As its thickness is proportional to $N_{surf}^{-1/2}$, it therefore decreases.[10,11] This phenomenon therefore leads to the sharp increase of $\Delta\varepsilon_3$ as here observed (eq. (S2) of Supporting Info S4).

For better accuracy, it is more suitable to use here Nyquist plots of conductivity to determine the conductivities of N0bS. The Nyquist plot of conductivity (i.e. σ" vs. σ') of N0bS at 294 K is shown in Figure 7a. In the low frequency part, two circular arcs (C1 and C2) show that the complex conductivity σ(ω) of N0bS is the sum of two relaxation functions:

$$\sigma(\omega) = \frac{\sigma_{cs} - \sigma_{ss}}{1+(i\omega\tau_2)^{1-\alpha_2}} + \frac{\sigma_{ss} - \sigma_{sol/s}}{1+(i\omega\tau_1)^{1-\alpha_1}} \quad (7)$$

where $\sigma_{sol/s}$ is the conductivity of the whole N0bS sample taking account of adsorbed solvent molecules on its entire surface. σ_{ss} and σ_{cs} are the NMC sample (i.e. set of NMC clusters) and cluster conductivities, respectively. Hence, an insulating gap (PVdF + EC:DMC) gives rise to the contact resistance/capacitance which generate the conductivity relaxation C1. The NMC sample conductivity σ_{ss} is determined by the crossing of high frequency part of C1 with the real axis. The relaxation domain C2 obtained after subtracting C1 corresponds to the inter-cluster contact resistance/capacitance. The cluster conductivity σ_{cs} is determined by the crossing of high frequency part of C2 with the real axis. Fig. 7b shows that the conductivities of N0bS, which are compared with that of N0b, are thermally activated above the freezing temperature (i.e. $T_F \approx 278$ - 279 K) of EC:DMC. The conductivities of N0bS are higher than

that of N0b: the cluster conductivity is increased by a factor of 2 while that of the sample (set of clusters) is five times more raised. Moreover, cluster and sample conductivities have the same activation energies of about 0.23 eV. This confirms that the inter-cluster electronic transfers are facilitated by the presence of EC dipoles near the contacts between clusters. Therefore, the surface potential is negligible and most likely less than 0.01 eV which is consistent with a lower space-charge thickness in the presence of adsorbed EC strong dipoles, hence a large increase in the sample conductivity. Note that the increase in the conductivity of the cluster from 1.0 to 1.9 $S.m^{-1}$ (at 296 K) obviously influences that of the sample. This increase of the cluster conductivity seems surprising considering the size of the cluster (i.e. 5 μm). A simplistic approach for cluster conductivity and resistivity allows to understand the increase of the NMC cluster conductivity σ_{cs} with EC:DMC. The total resistance R_c from one edge of the cluster to the other (in N0b), which is inversely proportional to $\sigma_c = \rho_c^{-1}$, can be approximated to the sum of its core resistance R_c^{core} and its surface resistance R_c^{surf} that is to say:

$$R_c = R_c^{core} + R_c^{surf} \quad (8)$$

The surface is distinguished from the core as the surface is influenced by the NMC/EC:DMC interactions. Let w be the thickness of the surface layer (or space-charge thickness) and D the cluster diameter, the core size is approximately equal to D since D >> w. By giving an arbitrary value equal to 1 for the area of the two resistances, the total resistivity of the NMC cluster in N0b is given by,

$$\rho_c = \rho_c^{core} + \rho_c^{surf} \frac{2w}{D} \quad (9)$$

It has been previously seen that the polarization of the cluster gives rise to a dielectric relaxation whose strength $\Delta\varepsilon_3$ is inversely proportional to w ($\Delta\varepsilon_3 \propto w^{-1}$) (Supporting Info S4). As the hole (Ni^{3+}) concentration in the surface layer is $N_{surf} \propto w^{-2}$ (see Eq. S2 in Supporting

391 Information), the resistivity of the surface layer is given by $\rho_c^{surf} = Aw^2$ (A being a
392 constant). The expression 9 is thus reduced to

393 $$\rho_c = \rho_c^{core} + Bw^3 \quad (10)$$

394 where Bw^3 corresponds to the surface "resistance" of the cluster with B = 2A/D. The core
395 resistivity ρ_c^{core} (or R_c^{core}) does not undergo surface interactions because D >> w. The
396 comparison of the resistivities of N0b and N0bS will allow the calculation of ρ_c^{core}. When the
397 sample is filled with EC:DMC (sample N0b), the surface layer thickness, the dielectric
398 strength and the cluster resistivity become w_S, $\Delta\varepsilon_{3S}$ and ρ_{CS} respectively. Comparing the
399 dielectric strengths $\Delta\varepsilon_3$ = 110 and $\Delta\varepsilon_{3S}$ = 378, the surface thickness becomes w_S = w/3.44. As
400 the total cluster resistivities are ρ_c = 1 Ω.m and ρ_{cs} ≈ 0.53 Ω.m at RT, the expression (10)
401 applied to N0b and N0bS gives: $\sigma_c^{core} = 1/\rho_c^{core}$ ≈ 1.9 S.m^{-1} with Bw^3 = 0.48 Ω.m and Bw_S^3
402 ≈ 0.01 Ω.m. The total conductivity of the cluster tends towards its core conductivity in the
403 presence of EC:DMC on its surface (Table 2). This surprising result shows that the presence
404 of EC:DMC at NMC surface leads to a sharp drop in cluster surface resistance, from 0.48 to
405 0.01 Ω.m, then becoming negligible. The five times increase of the sample (set of clusters)
406 conductivity ($\sigma_{ss}/\sigma_s \approx 5$) could be attributed to a significant decrease of the contact resistance
407 at the clusters junctions as a consequence of the decrease of the surface resistance of the
408 clusters. Below the freezing temperature T_F, the sample σ_{ss} conductivity drops by about an
409 order of magnitude and the cluster conductivity σ_{cs} decreases slightly toward what it would be
410 with the dry sample (Fig. 7b). EC:DMC then acts as an inert solid dielectric and therefore
411 without interaction with NMC532 below T_F.

412 **3.5. Samples soaked by LP30.**

413 After showing how dipoles act with NMC, the ion / NMC interactions are studied by
414 introducing electrolyte LP30 into the pores of the dry compound N0b which will subsequently
415 become N0bE. The decomposition of Nyquist plots of permittivity (Fig. 8) shows the

existence of five circular arcs defining five relaxations (W1 to W5). The lowest frequency part of the dielectric spectrum is a giant relaxation (W1) which only exists above the freezing temperature T_F of the electrolyte. The W1 relaxation therefore has an ionic origin and can be attributed to an ionic double-layer at the sample electrolyte interface. Its characteristic frequency ν_1 = 30 Hz at 295 K is thermally activated with an activation energy of about 0.24 eV. The mean dielectric strength $\Delta\varepsilon_1 = 1.21\times10^7$ of W1 is not dependent on the temperature above T_F. The values of ν_1 and $\Delta\varepsilon_1$ agrees with that *(i.e. frequency ≈ 42 Hz at RT and strength* $\approx 1.76\times10^7$*)* obtained for an electrode containing NMC333 and 1.8 wt% of carbon black. **Erreur ! Signet non défini.** As the permittivity of the sample filled with electrolyte (i.e. $\varepsilon_{SE} \approx 9000$) is negligible compared to that of the whole sample/double layer *(i.e.* $\varepsilon_{SE} << (\varepsilon_{SE} + \Delta\varepsilon_1) \approx 1.21\times10^7$*)*, the double layer capacitance per unit surface area is given by

$$C_{dl} \approx \frac{\varepsilon_0 \Delta\varepsilon_1}{L_s} \quad (11)$$

where $L_s \approx 400$ μm is the sample thickness. The Equation (11) yields $C_{dl} = 20$ μF.cm^{-2} according to the order of magnitude generally obtained for electrode materials in batteries. [5] The W2 relaxation is evidenced after subtraction of the W1 contribution from the whole spectrum. The other relaxations W3, W4 and W5 are also determined after subtractions of W2, W3 and W4, respectively. The relaxation frequency ν_2 *($\nu_2 = 4.2\times10^4$ Hz at 295 K)* of W2 is thermally activated on either side of the freezing temperature T_F of the electrolyte (Fig. 9a). The activation energy of ν_2 is around 0.25 eV for $T > T_F$ in the liquid state, while it is higher of about 0.44 eV for $T > T_F$ in the solid state. The dielectric strength $\Delta\varepsilon_2$ *($\Delta\varepsilon_2 = 7400$ at 295 K)* of W2 decreases moderately above T_F and then drops below T_F (Fig. S51). The relaxation W2 is thus attributed to local ion motions in the electrolyte because of the significant modification of their dynamics at the freezing temperature T_F. It should be noted that the W2 relaxation is similar to that evidenced for an electrode containing NMC333 and

1.8 % of carbon black. **Erreur ! Signet non défini.** The two relaxations W3 and W4, which have characteristic frequencies $\nu_3 = 10^6$ Hz and $\nu_4 = 1.5\times10^7$ Hz, are of the same order than that of the relaxations P2 and P3 for N0b and N0bE at room temperature (Table 1, Fig. 6c and S31). W3 and W4 are thus electronic space-charge relaxations respectively attributed to sample (set of clusters) and cluster polarizations as in N0b and N0bE. They are thermally activated with activation energies $E_3 = E_4 = 0.23$ eV. Looking at the intrinsic properties of NMC (i.e. the NMC cluster), we find that the frequency prefactor $\nu_{04} = 1.5\times10^{11}$ Hz of ν_4 is quasi-similar to that of N0b ($= 2\times10^{11}$ Hz, Table 1) and of N0bE ($= 3\times10^{11}$ Hz, Fig. 6c). These relaxations are thus associated to hole motions from either side of NMC cluster boundaries, whether the material is wet or dry. The dielectric strength $\Delta\varepsilon_4$ of W4 is also higher than the dielectric strength of P3, since they are equal to 678 instead of 110 and 378 for N0b and N0bS, respectively. This increase of $\Delta\varepsilon_3$ is amplified compared to N0b and N0bS because the ions (i.e. mostly PF_6^- anions) adsorbed in addition to the EC dipoles tend thus to attract more charges towards the cluster surface. This leads to a supplementary increase of the Ni^{3+} content N_{surf} in the space-charge layer whose thickness becomes even smaller. It will be shown later that this phenomenon has consequences for the conductivity.

As ion and electron flows are carried out in parallel, it is more obvious to use Nyquist plots of complex conductivity (σ" vs. σ'). **Erreur ! Signet non défini.** The Nyquist plots of N0bS at 294 K are shown in Figure 10a-c. In the low frequency part, a circular arc C1 (Fig. 10a), which crosses the real axis σ' at $\sigma_{se} \approx 0$ (given the accuracy of measurements) and σ_{si}, corresponds to a blocking interface between an ionic conductor (i.e. LP30 electrolyte within the pores) and the gold collector. The electric equivalent circuit is an ionic double layer capacity in series with a resistance proportional to the inverse of the conductivity σ_i (Fig. 10a). Once the contribution C1 is subtracted, a second circular arc C2 (Fig. 10b) is an arc of circle crossing the real axis σ' at σ_{si} and σ_i. A third contribution C3 (Fig. 10c), which is

465 evidenced by subtracting C1 and C2, crosses the real axis σ' at σ_i and σ_T. Figure 10d shows
466 that σ_{si} and σ_i are thermally activated above T_F with activation energies of about 0.27 eV and
467 0.24 eV, respectively. Below T_F, σ_{si} and σ_i drop sharply and become similar with the decrease
468 of the temperature (Fig. 10d). Consequently, σ_{si} and σ_i are conductivities due to ionic
469 transfers (Li^+ and PF_6^-) within the electrolyte filling the pore network. The conductivity
470 relaxation C2 can be attributed to forward-backward ion motions caused by the existence of
471 pore tortuosity. The latter involve ionic concentration gradients producing some coulombic
472 repulsions between charges of the same sign at junctions of the pore segments. Another
473 hypothesis would suggest that the adsorption-desorption of the ions from NMC surface could
474 also increases the number of repulsions. The existence of such interactions justifies the higher
475 activation energy of about +0.03 eV for σ_{si}. One part of cations and anions could move in the
476 same direction because of significant correlations between their motions. [20] The smaller
477 conductivity σ_{si} is thus the bulk ionic conductivity which is composed of a set forward-
478 backward movements. [21] Hence, the larger conductivity σ_i would be the ionic conductivity
479 free from backward ionic movements, which would be directly linked to auto diffusion
480 coefficients of Li^+ and PF_6^- ions.

481 The relations between the liquid electrolyte conductivity σ_{lp30} and the conductivities
482 σ_{si} and σ_i can be provided by the Archie's law:

483 $$\sigma_{si} = \sigma_{lp30}\phi^m \quad (12a)$$

484 $$\sigma_i = \sigma_{lp30}\phi^{m\prime} \quad (12b)$$

485 where ϕ is the porosity volume fraction of the sample filled with the electrolyte. The two
486 exponents m and m' are related to the geometry of the pores network and especially to their
487 tortuosity. Equations (12a) and (12b) lead to m = 2.5 and m' = 2, with ϕ = 0.264, σ_{lp30} = 1.2

488 $S.m^{-1}$, σ_{si} = 4.5×10^{-2} $S.m^{-1}$ and σ_i = 8×10^{-2} $S.m^{-1}$ at RT. The m' value agrees with that
489 determined by numerical simulation of the ionic conductivity of similar electrodes wetted by
490 the electrolyte LP30.[22] The later simulations could not consider coulombic repulsions and
491 forward-backward ion motions. The m value agrees with that determined by BDS for an
492 electrode containing NMC333 and 1.8 % of carbon black.[Erreur ! Signet non défini.] The theoretical
493 relationship between the tortuosity, the porosity, the ionic conductivity of the electrolyte
494 confined in the pores (σ_i) and that of the free electrolyte (σ_{lp30}) is given by

495 $$\frac{\sigma_i}{\sigma_{lp30}} = \frac{\phi}{T_p} \quad (13)$$

496 where T_p is the tortuosity factor. Equation (13) leads to $T_p \approx 3.96$ by using $\phi = 0.264$, σ_{lp30} =
497 1.2 $S.m^{-1}$ and σ_i = 0.08×10^{-2} $S.m^{-1}$ at RT. This value is in very good agreement with other
498 simulations of ion diffusive properties in typical NMC-based electrodes, [23] and with diffusion
499 experiments, but on $LiFePO_4$- and $LiCO_2$- based electrodes. [24,25] It should be noted that the
500 activation energy of σ_i (i.e. E_i) is equal to 0.24 eV instead of 0.21 eV for that of σ_{lp30} (i.e.
501 E_{lp30}) [26,27] implying a temperature dependence of the tortuosity factor T_p. This aspect has
502 never been discussed for battery materials, to the best of our knowledge, and deserves
503 complementary studies.

504 The conductivity C3 relaxation permits to obtain the electronic NMC cluster
505 conductivity σ_{CE} = (σ_T – σ_i) since electronic and ionic fluxes are parallel. The cluster
506 conductivity of N0bE, which is σ_{CE} = 1.6 $S.m^{-1}$ at 295 K, follows an Arrhenius law with an
507 activation energy equal to 0.23 eV. This conductivity is higher than the cluster conductivity
508 σ_C in the N0b (i.e. 1 $S.m^{-1}$ at room temperature) but nearly similar to that of N0bS (i.e. 1.9
509 $S.m^{-1}$ at room temperature). The increase of the cluster conductivity of N0bE due to adsorbed
510 ions can be understood by using the expression (10). The surface layer thickness, the
511 dielectric strength and the cluster resistivity of N0bE are here w_E, $\Delta\varepsilon_{3E}$ and ρ_{CE} respectively.

Comparing the respective dielectric strengths $\Delta\varepsilon_3$ = 110 and $\Delta\varepsilon_{3S}$ = 678 of N0b and N0bE, the surface thickness becomes w_E = w/6.16. Knowing the resistivities of N0b (ρ_C ≈ 1 Ω.m at RT) and of N0bE (ρ_{CE} ≈ 0.62 Ω.m at RT), the expression (10) gives $\sigma_c^{core} = 1/\rho_c^{core} \approx 1.6$ S.m^{-1} with surface resistances Bw^3 = 0.48 Ω.m and $Bw_E{}^3 \approx 0.0016$ Ω.m. The total conductivity of the cluster tends towards its core conductivity, as for N0bS (Table 2). The presence of adsorbed ionic (mainly PF_6^- anions) species on the cluster surface makes its surface resistance negligible, as in the presence of only EC dipoles. However, the drop in cluster surface resistance is more significant in the presence of the ions (Bw^3 = 0.48 Ω.m in N0b, $Bw_S{}^3 \approx$ 0.01 Ω.m. in N0bS and $Bw_E{}^3 \approx 0.0016$ Ω.m. in N0bE).

4. CONCLUSIONS

BDS showed for the first time the influence of interfaces in the charge transport phenomena of $LiNi_{0.5}Mn_{0.3}Co_{0.2}O_2$ (NMC532). The interfaces (solid/solid and solid/liquid) are at the origin of space charges which then induce polarizations at all size scales inside the NMC532/PVdF composite. BDS provides both information on electron transfers (above about 10^6 Hz) as well as information on ion diffusion into the electrolyte filling the sample pore network (below about 10^5 Hz). By way of summary, Figure 11a summarizes the activation energy as a function of the relaxation frequency at 295 K of the three types of polarizations that it was possible to discriminate: ionic transfers at the lowest frequencies, electronic transfers and dipole rotations at the highest frequencies. The dynamics of electronic transfers at the size scales of clusters and particles are correlated in NMC532, but also in NMC333. In all cases, these are hole transfers at a frequency of 3×10^{11} Hz (i.e. transfer time ~0.53 ps) between two neighboring nickel ions (Fig. 11b). The electronic conductivity of NMC532 is much higher than that of NMC333, at all size scales, due to the percolation of Ni^{3+}/Ni^{2+} ions in greater quantity in NMC532. These are the energetic barriers (i.e. activation energies) that

differentiate the electronic transfers between the different size scales. These energy barriers are mainly due to the various interfaces within the composite material: grain boundaries between particles forming clusters, contacts between clusters forming the conductive matrix and surfaces of the clusters in contact with the electrolyte (dipoles and adsorbed ions). Since NMC is a p-type semiconductor, the adsorption of negatively charged species, namely anions and PF_6^- and EC dipoles oriented toward the liquid phase is favored. The attractive coulombic interactions between the EC dipoles or the PF_6^- anions and the holes, increase the amount of Ni^{3+} at the surface of the NMC and thus increase the conductivity at the surface of the NMC. This promotes electronic transfers (holes) in the NMC at all scales (particles, clusters, composite), as illustrated in Figure 11b.

On the other hand, the ionic conductivity was measured. The microstructure of the composite hinders ionic transfers. There are certainly forward-backward movements due to coulombic repulsions between ions of the same sign. These interactions are probably due to the existence of an ionic concentration gradient due to the tortuosity of the pores and / or to ionic movements of adsorption-desorption. The ionic conductivity value is then lower than it should be if it were truly diffusive. This shows that BDS is a powerful technique for detecting this type of phenomenon in porous composite materials. In order to complement this study from a theoretical view-point, additional computational studies could be of interest, including tight binding theory in semiconducting materials as well as tortuosity modelling in order to support the hypothesis of ionic motion limitation within the complex architecture electrode.

ACKNOWLEDGMENTS

We are grateful to the ANR for the funding of the Pepite project (ANR-15-CE05-0001).

Table 1.Electronic transfers and polarizations at different size levels of different NMC-based samples *(NMC sample, NMC cluster, NMC particle and NMC at interatomic scale)*: N0 *(this study)*, N0b *(this study)* and MX3 *(K.A. Seid et al. [3])*. Conductivities σ *(in S.m^{-1})*, dielectric strengths $\Delta\varepsilon$ and dielectric relaxation frequencies ν (in Hz) at room temperature; activation energies E *(in eV)* and dielectric frequency prefactors ν_0 *(in Hz)*.

Composite Materials	**N0** *NMC532* $LiNi_{0.5}Mn_{0.3}Co_{0.2}O_2$	**N0b** *NMC532* $LiNi_{0.5}Mn_{0.3}Co_{0.2}O_2$	**MX3** [3] *NMC333* $LiNi_{1/3}Mn_{1/3}Co_{1/3}O_2$
NMC volume fraction (%)	63	68.6	66
PVdF volume fraction (%)	3	5	7
Porosity (%)	34	26.4	27
NMC cluster diameter (μm)	5	5	3
Conductivity			
[(a)]Sample/PVdF σ_{Sb} (S.m^{-1}) E_{Sb} (eV)	***Non-existent***	4.1×10^{-4} 0.27	***Non-existent***
[(a)]Sample σ_S (S.m^{-1}) E_S (eV)	1.4×10^{-3} 0.25	3.8×10^{-3} 0.26	3.0×10^{-5} 0.30
Cluster σ_c (S.m^{-1}) E_c (eV)	5.0×10^{-1} 0.23	1.0 0.24	2.0×10^{-4} 0.25
Particle σ_P (S.m^{-1}) E_P (eV)	1.0×10^{2} 0.10	***Undefined***	2.0×10^{-1} 0.12
Interatomic σ_0 (S.m^{-1}) E_0 (eV)	***Undefined***	***Undefined***	1.9×10^{1} 0.00
Sample polarization (NMC/PVdF/Au)	***Non-existent***	2.0×10^{4}	***Non-existent***
ν_{2b} (Hz)		307	
$\Delta\varepsilon_{2b}$			
Sample polarization (NMC/Au)			
ν_2 (Hz)	1.6×10^{5}	5.0×10^{5}	2.0×10^{3}
$\Delta\varepsilon_2$	179	60	429
NMC cluster polarization			
ν_3 (Hz)	6.6×10^{7}	7.0×10^{7}	1.80×10^{7}
E_3 (eV)	0.20	0.20	0.25
ν_{03} (Hz)	2.0×10^{11}	2.0×10^{11}	3.3×10^{11}
$\Delta\varepsilon_3$	63	110	48
NMC particle polarization			
ν_4 (Hz)	6.4×10^{9}		2.6×10^{9}
E_4 (eV)	0.09	***Undefined***	0.11
ν_{04} (Hz)	2.0×10^{11}		2.6×10^{11}
$\Delta\varepsilon_4$	1.4		2.4

(a) Sample is defined here as a set of NMC clusters. The global dc-conductivity of N0b (σ_{Sb}) include a gap of PVdF between Au metallization and NMC sample. Global dc-conductivities of N0 and MX3 (σ_S) correspond to that of the NMC samples.

572 Table 2. Long- and short-range ionic conductivities of electrolyte LP30 filling the pores of the composite
573 samples. Effective total and core conductivities σ_C, σ_{CS} and σ_{CE} of NMC532 clusters in N0b (NMC532: 68.6 %;
574 PVdF: 5%; porosity: 26.4 %), N0bS *(NMC532: 68.6 %; PVdF: 5%; EC:DMC: 26.4 %)* and N0bE *(NMC532: 68.6 %;*
575 *PVdF: 5%; LP30: 26.4 %)* respectively at 295 K.

Sample	**Ionic conductivity** ***Long-range*** σ_{si} (S.m^{-1}) E_i (eV) ***Short-range*** σ_i (S.m^{-1}) E_i (eV)	**NMC sample conductivity** σ_S (S.m^{-1}) E_S (eV)	**NMC cluster conductivity** ***Total*** [(a)]σ_C (S.m^{-1}) E_C (eV) ***Core*** σ_C (S.m^{-1}) E_C (eV)
N0b	*Non-existent*	3.8×10^{-3} 0.26	1.0 0.24
	Non-existent		[(b)]1.6-1.9 0.24
N0bS	*Non-existent*	2.4×10^{-2} 0.23	1.9 0.23
	Non-existent		1.9 0.23
N0bE	4.3×10^{-2} 0.27	[(c)] *Not well defined*	1.6 0.23
	8.0×10^{-2} 0.24		1.6 0.23

576 *(a) Subscripts S and C are not written to simplify*
577 *(b) Calculated value from expression (10).*
578 *(c) Conductivity probably of the same order of magnitude of that of N0bS. The sample conductivity cannot be*
579 *determined precisely because a non-negligible ionic conductivity and a higher NMC cluster conductivity.*

580

581

582

583

FIGURE CAPTIONS

Fig. 1. a) Schematic description of the different sources of polarization at different size levels of samples. b) SEM images of NMC532 clusters and particles. c) EDS spectrum analysis (0-8 keV) of NMC532. d) X-ray diffraction patterns of NMC532. e) Schematic structure of NMC532.

Fig. 2. Frequency dependent: (a) real part of conductivity σ', (b) real part of permittivity ε' and (c) imaginary part of permittivity ε" of dry samples N0 (NMC532: 63%; PVdF: 3%; porosity: 34%) and N0b (NMC532: 68.6 %; PVdF: 5%; porosity: 26.4 %) at 293 K.

Fig. 3. a) Nyquist plots of complex permittivity, ε"(ω) vs. ε'(w) of dry N0b (NMC532: 68.6 %; PVdF: 5%; porosity: 26.4 %) at 293 K: low-frequency part *(left plot)* described by a straight line P1, dielectric relaxations P2b, P2 and P3 *(right plots)* obtained after subtracting contributions P1, P2b and P2 successively *(Table 1)*. b) Dielectric relaxation frequency ν_3 of P3 *(NMC532 cluster polarization)* as function of inverse temperature. c) Nyquist plot (low-frequency part) of complex resistivity, ρ"(ω) vs. ρ'(ω) of dry N0b and determination of the conductivities and σ_s at 293 K (Table 1). d) Higher frequency part of σ_{sb} complex resistivity plot at 293 K and determination of the conductivity σ_c (Table 1). e) Arrhenius plots of conductivity: sample/PVdF (σ_{sb}) (●), sample (σ_s) (●) and cluster (σ_c) (●).

Fig. 4. a) Real parts of conductivity (σ') and permittivity (ε') as a function of the frequency for dry sample (N0b), sample filled by EC:DMC (N0bS) and sample filled by LP30 (N0bE) at room temperature. b) Histograms comparing conductivities (σ' at RT) of N0b, N0bS and N0bE at 10^2 Hz and 10^{10} Hz. c) Histograms comparing permittivities (ε' at RT) of N0b, N0bS and N0bE at 10^2 Hz.

606 **Fig. 5.** a) Nyquist plots of complex permittivity, ε”(ω) vs. ε’(ω) of sample filled by EC:DMC
607 1:1, i.e. N0bS (NMC532: 68.6 %; PVdF: 5%; EC:DMC: 26.4 %) at 293 K. a) Entire plot from
608 50 to 10^{10} Hz: only the low-frequency part contribution P1*(straight line)* is visible. b) Plot
609 obtained upon subtracting the contribution P1: evidence of the dielectric relaxation P2bs
610 *(circular arc)*. c) Plot obtained upon subtracting the contribution P2bs: evidence of the
611 dielectric relaxation P2s *(circular arc)*. d) Plot obtained upon subtracting the contribution
612 P2s: evidence of the dielectric relaxation P2b *(circular arc)*. e) Plots obtained upon
613 subtracting the contribution P2b: evidence of the dielectric relaxations P2 and P3 *(circular*
614 *arcs)*. f) Plot obtained upon subtracting the contribution P2 and P3: evidence of the dielectric
615 relaxation P5 *(circular arc)*.
616 **Fig. 6.** Influence of EC:DMC on: (a) frequencies and (b) dielectric strengths of the different
617 dielectric relaxations for dry sample N0b (■) and sample filled by EC:DMC (N0bS) (■)at 295
618 K. Influence of EC:DMC on Arrhenius plots of: (c) relaxation frequency ν_3 and (d) dielectric
619 strength $\Delta\varepsilon_3$ of cluster polarization for N0b (●) and N0bS (●).

620 **Fig. 7.** a) Conductivity Nyquist plots of N0bS (N0b filled by EC:DMC) at 296 K: low
621 frequency relaxation domain C1 (solvent / sample interface) and high frequency relaxation
622 domain C2 (inter-cluster of NMC) obtained after subtracting C1. b) Arrhenius plots of
623 different types of conductivity vs. inverse temperature (N0bS: full circles and N0b: full
624 squares): NMC cluster conductivity σ_{CS} (●) and σ_C (■), NMC sample conductivity σ_{SS} (●) and
625 σ_S (■), conductivity $\sigma_{sol/S}$ including PVdF/NMC interface (●) and sample/PVdF conductivity
626 σ_{sb} (■). The black arrow is the freezing temperature of EC:DMC.

627 **Fig. 8.** a) Nyquist plots of complex permittivity, ε”(ω) vs. ε’(ω) of sample filled by LP30, i.e.
628 N0bE (NMC532: 68.6 %; PVdF: 5%; LP30: 26.4 %) at 295 K. a) Low-frequency part of the
629 plot: evidence of the giant dielectric relaxation domain W1 *(semi-circle)*. b) Plot obtained

upon subtracting the contribution W1: evidence of the dielectric relaxation W2 *(circular arc)*. c) Plot obtained upon subtracting the contribution W2: evidence of the dielectric relaxation W3 *(circular arc)*. d) Plot obtained upon subtracting the contribution W3: evidence of the dielectric relaxation W4 *(circular arc)*. e) Plot obtained upon subtracting the contribution W4: evidence of the dielectric relaxation W5 *(circular arc)*. Electrolyte LP30: 1 M of LiPF6 EC:DMC 1:1.

Fig. 9. (a) Relaxation frequency ν_2 of ionic motions in N0bE. (b) Comparisons of relaxation frequencies ν_4 of NMC cluster polarization at RT. (c) Temperature dependence of dielectric strengths $\Delta\varepsilon_4$ of NMC cluster polarization for sample N0bE filled by LP30 (•)and for dry sample N0b (•). (d) Relaxation frequency ν_5 of EC dipole rotation vs. inverse temperature.

Fig. 10. Nyquist plots of the imaginary part $\sigma''(\omega)$ vs. the real part $\sigma'(\omega)$ of the complex conductivity of NMC532 filled by LP30 (N0bE) at 295 K: a) low frequency part of the spectrum and evidence of the relaxation domain C1 (arc of circle); b) plot obtained upon subtracting C1 and evidence of the relaxation domain C2 (arc of circle); c) plot obtained upon subtracting C2 and evidence of the relaxation domain C3 (arc of circle). σ_{si} = bulk ionic conductivity, σ_i = local (or diffusive) ionic conductivity, σ_{CE} = NMC532 cluster conductivity and $\sigma_T = \sigma_I + \sigma_{CE}$. Arrhenius plots of: d) ionic conductivities σ_{si} and σ_i, and e) NMC532 cluster (electronic) conductivity σ_{CE}.

Fig. 11. a) Activation energies vs. relaxation frequencies at 295 K attributed to: ionic motions (Li^+, PF_6^-) in pore network filled with LP30, solvent dipole rotations (i.e. EC) and electronic motions (i.e., holes) in clusters and particles of NMC532 and NMC333. [5] The slope of the dotted line with an arrow is kTln10 with T = 295 K and gives an average frequency prefactor around 3×10^{11} Hz (for electronic motions). b) Influence of adsorbed solvent dipoles (EC in EC:DMC and LP30) and ions (PF_6^- in LP30) on total resistivity of NMC532 clusters. The

654 drop of the total resistivity is proportional to the mean surface resistance of the cluster of the
655 dry compound N0b. at zero activation energy. Symbols used: dry NMC333 (■) [5], dry
656 NMC532 or N0b (■), NMC 532 filled with EC:DMC or N0bS (■) and NMC 532 filled with
657 LP30 or N0bE (■).

658

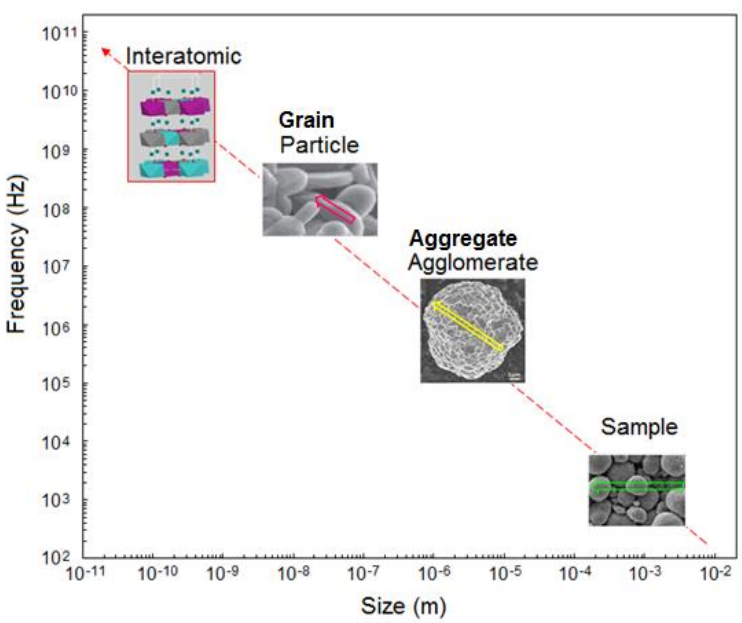

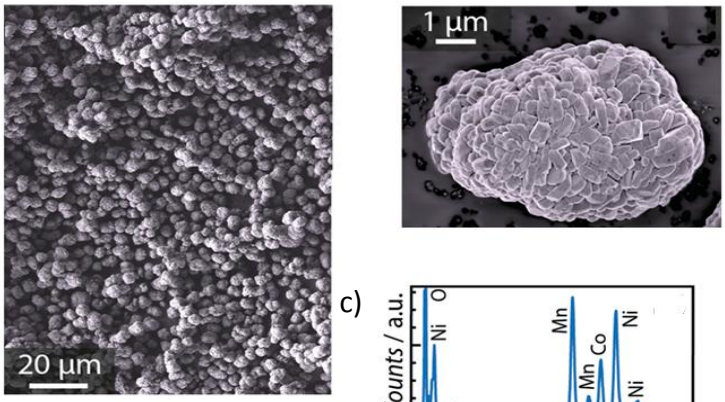

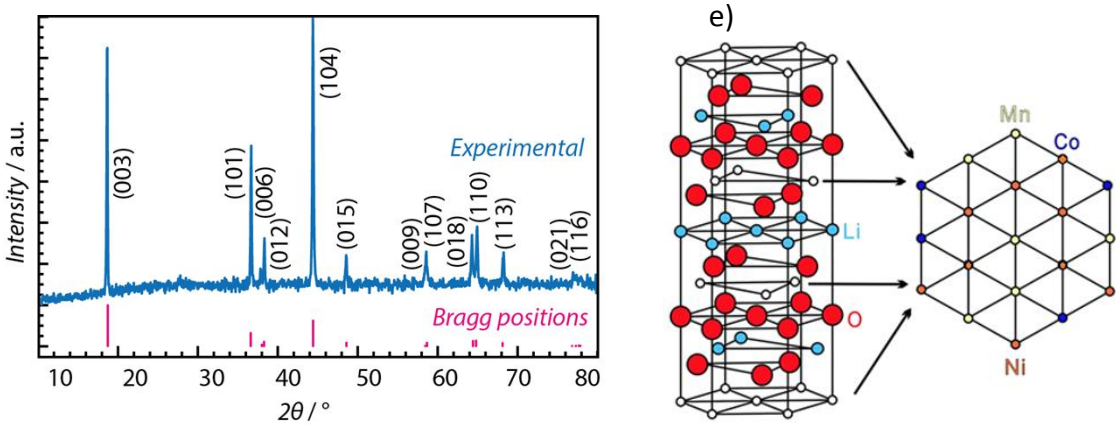

Fig. 1. a) Schematic description of the different sources of polarization at different size levels of samples. b) SEM images of NMC532 clusters and particles. c) EDS spectrum analysis (0-8 keV) of NMC532. d) X-ray diffraction patterns using a PANalytical XPert Pro diffractometer: Cu-Kα: λ=1.5408Å and step size of 0.017°.s^{-1}. e) Schematic structure of NMC532.

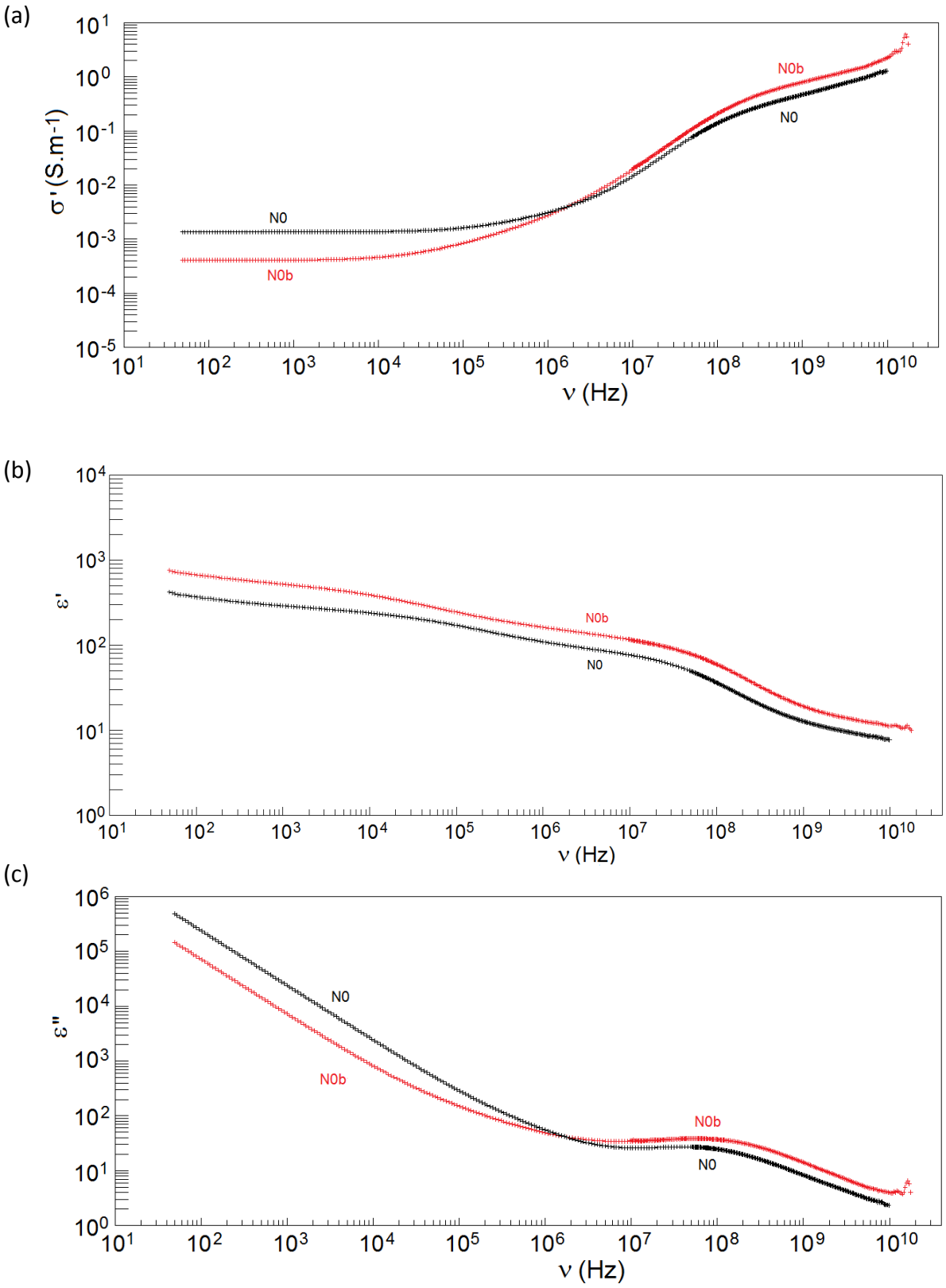

Fig. 2. Frequency dependent: (a) real part of conductivity σ', (b) real part of permittivity ε' and (c) imaginary part of permittivity ε" of dry samples N0 (NMC532: 63%; PVdF: 3%; porosity: 34%) and N0b (NMC532: 68.6 %; PVdF: 5%; porosity: 26.4 %) at 293 K.

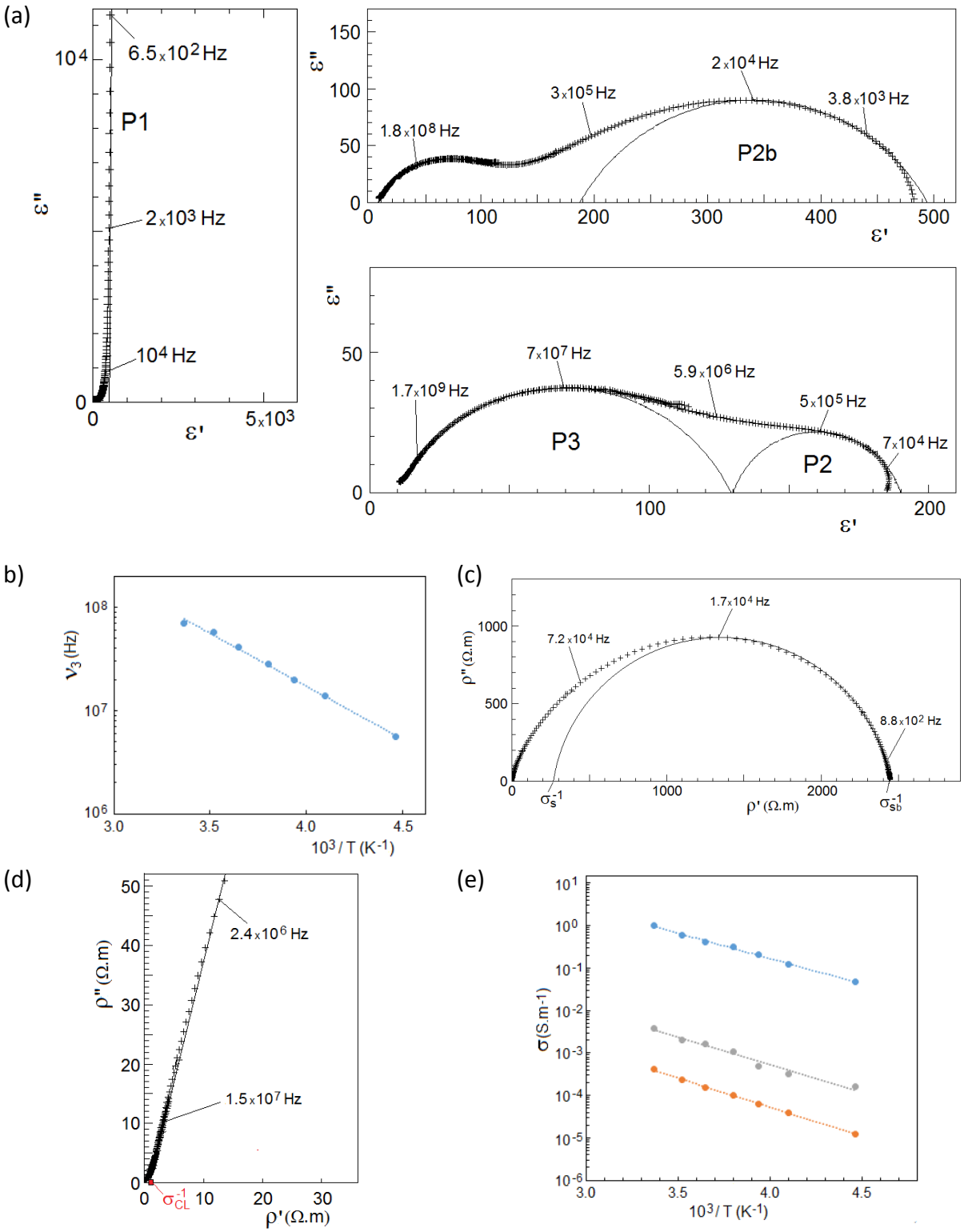

Fig. 3. a) Nyquist plots of complex permittivity, ε"(ω) vs. ε'(w) of dry N0b (NMC532: 68.6 %; PVdF: 5%; porosity: 26.4 %) at 293 K: low-frequency part *(left plot)* described by a straight line P1, dielectric relaxations P2b, P2 and P3 *(right plots)* obtained after subtracting contributions P1, P2b and P2 successively *(Table 1)*. b) Dielectric relaxation frequency ν_3 of P3 *(NMC532 cluster polarization)* as function of inverse temperature. c) Nyquist plot (low-frequency part) of complex resistivity, ρ"(ω) vs. ρ'(ω) of dry N0b and determination of the conductivities and σ_s at 293 K (Table 1). d) Higher frequency part of σ_{sb} complex resistivity plot at 293 K and determination of the conductivity σ_c (Table 1). e) Arrhenius plots of conductivity: sample/PVdF (σ_{sb}) (●), sample (σ_s) (●) and cluster (σ_c) (●).

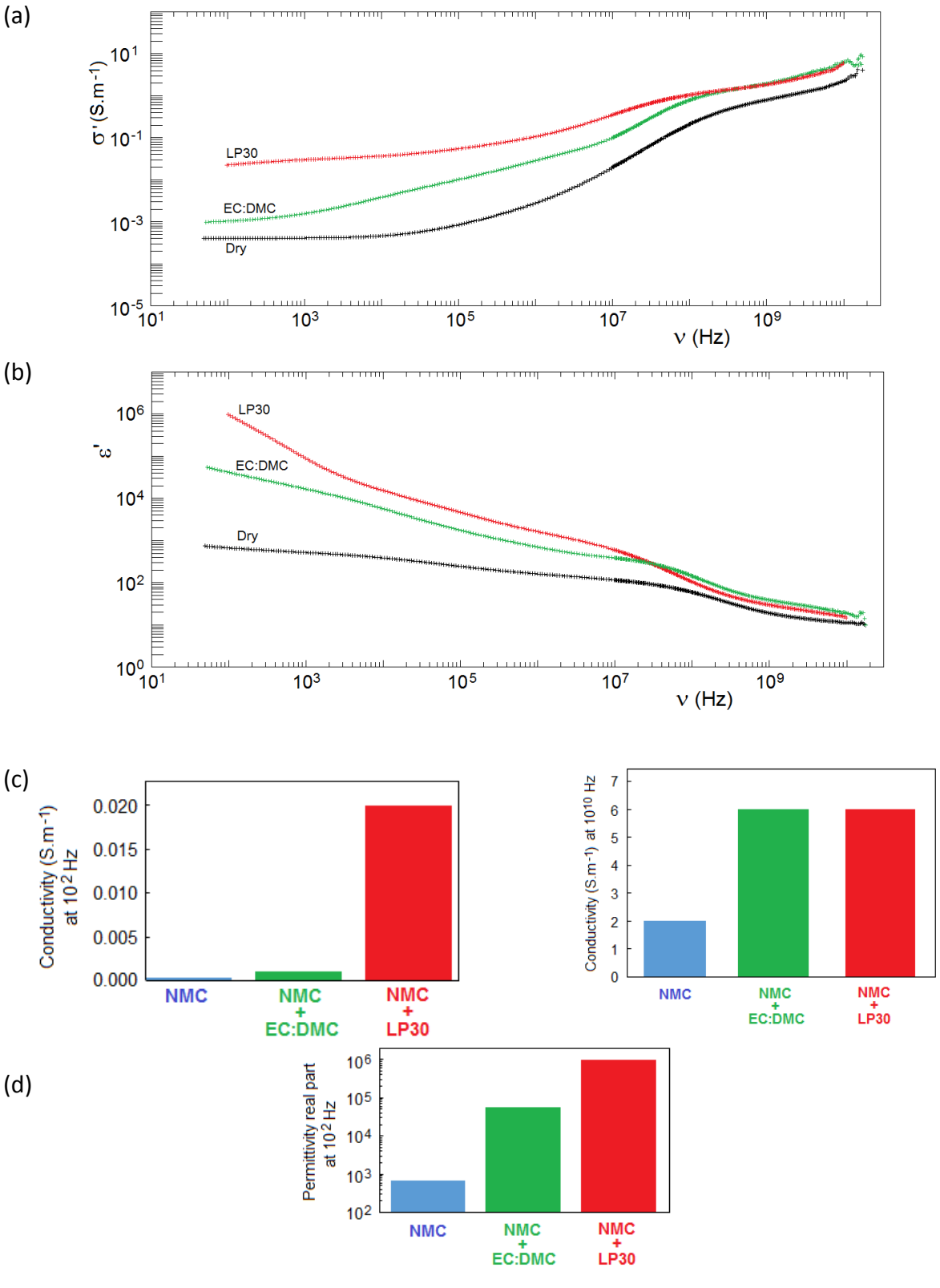

Fig. 4. a) Real parts of conductivity (σ') and permittivity (ε') as a function of the frequency for dry sample (N0b), sample filled by EC:DMC (N0bS) and sample filled by LP30 (N0bE) at room temperature. b) Histograms comparing conductivities (σ' at RT) of N0b, N0bS and N0bE at 10^2 Hz and 10^{10} Hz. c) Histograms comparing permittivities (ε' at RT) of N0b, N0bS and N0bE at 10^2 Hz.

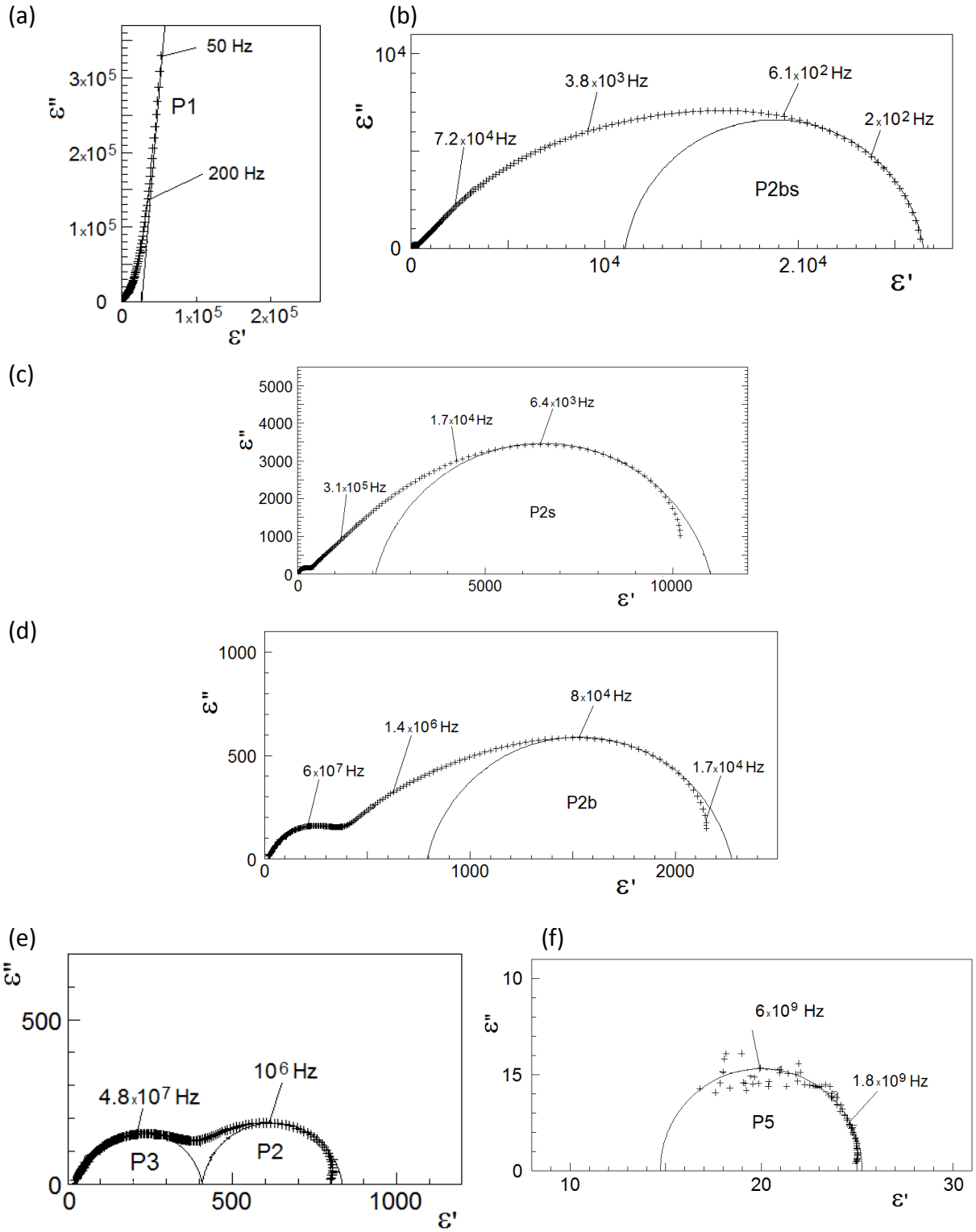

Fig. 5. a) Nyquist plots of complex permittivity, ε”(ω) vs. ε’(ω) of sample filled by EC:DMC, i.e. N0bS (NMC532: 68.6 %; PVdF: 5%; EC:DMC: 26.4 %) at 293 K. a) Entire plot from 50 to 10^{10} Hz: only the low-frequency part contribution P1*(straight line)* is visible. b) Plot obtained upon subtracting the contribution P1: evidence of the dielectric relaxation P2bs *(circular arc)*. c) Plot obtained upon subtracting the contribution P2bs: evidence of the dielectric relaxation P2s *(circular arc)*. d) Plot obtained upon subtracting the contribution P2s: evidence of the dielectric relaxation P2b *(circular arc)*. e) Plots obtained upon subtracting the contribution P2b: evidence of the dielectric relaxations P2 and P3 *(circular arcs)*. f) Plot obtained upon subtracting the contribution P2 and P3: evidence of the dielectric relaxation P5 *(circular arc)*.

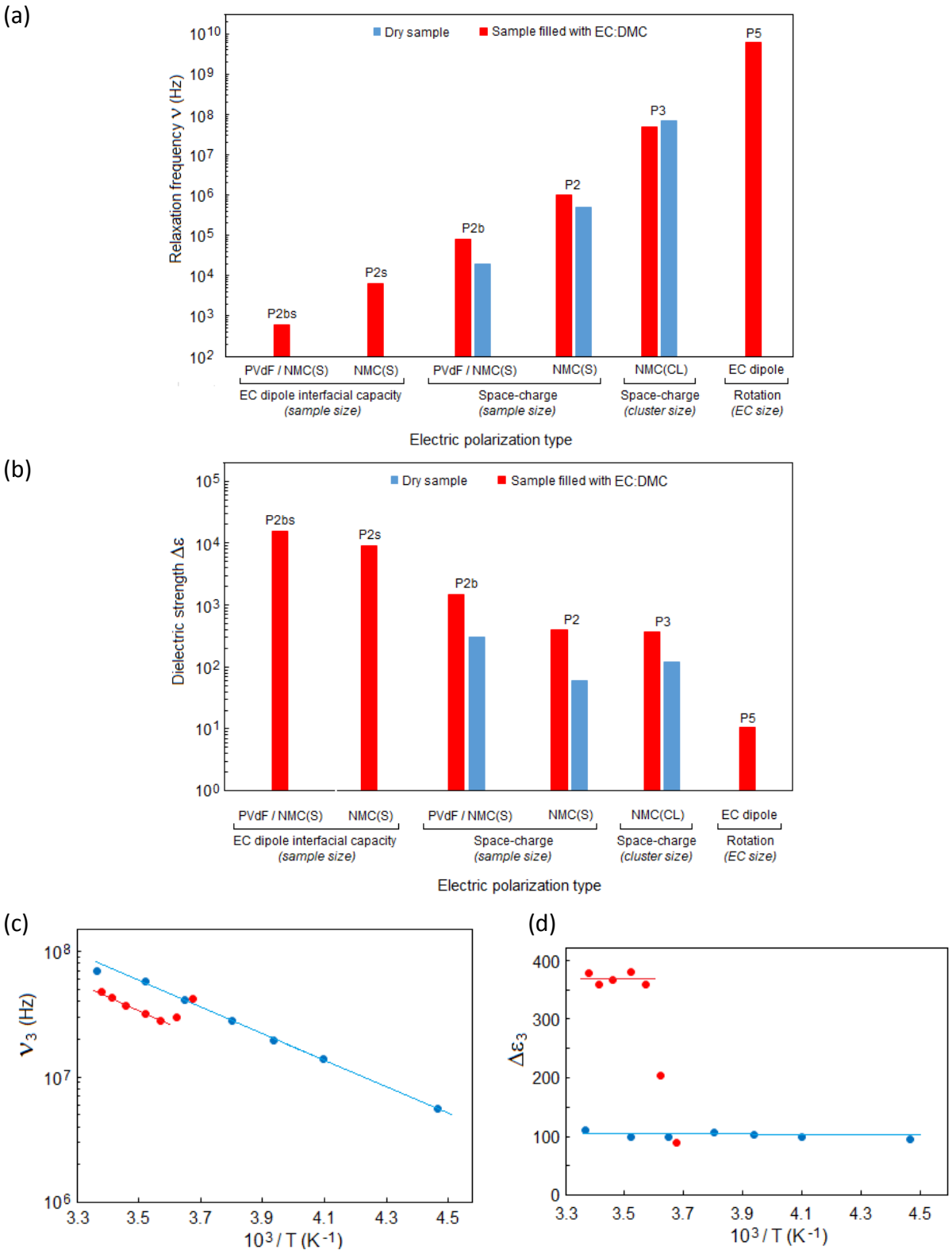

Fig. 6. Influence of EC:DMC on: (a) frequencies and (b) dielectric strengths of the different dielectric relaxations for dry sample N0b (■) and sample filled by EC:DMC 1:1 (N0bS) (■)at 295 K. Influence of EC:DMC on Arrhenius plots of: (c) relaxation frequency ν_3 and (d) dielectric strength $\Delta\varepsilon_3$ of cluster polarization for N0b (•) and N0bS (•)

848

(a)

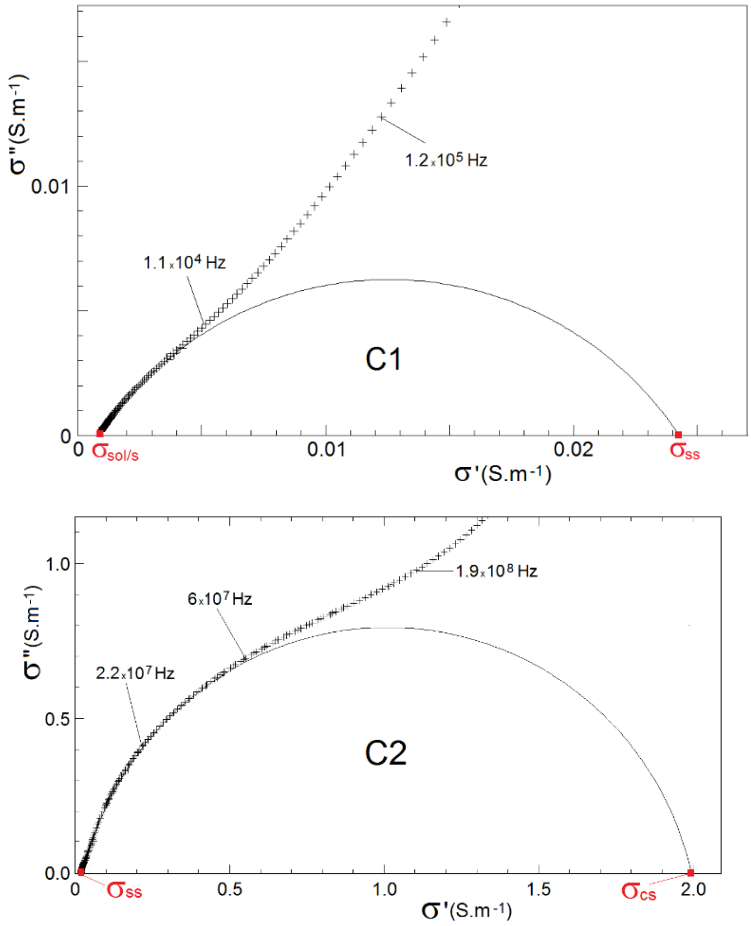

b)

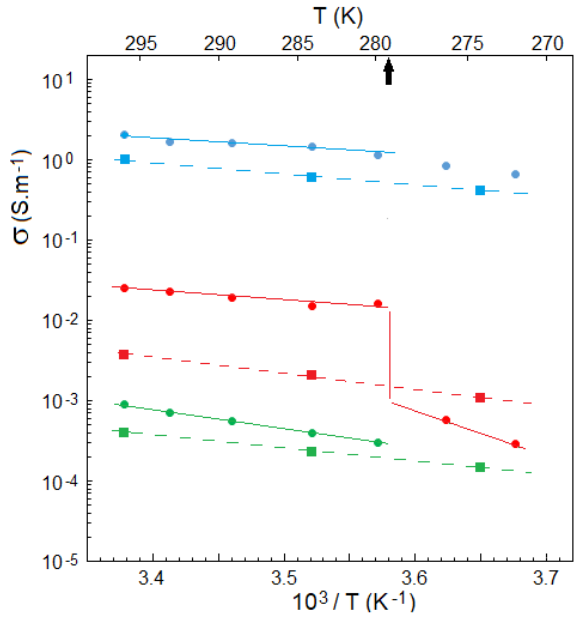

Fig. 7. a) Conductivity Nyquist plots of N0bS (N0b filled by EC:DMC) at 296 K: low frequency relaxation domain C1 (solvent / sample interface) and high frequency relaxation domain C2 (inter-cluster of NMC) obtained after subtracting C1. b) Arrhenius plots of different types of conductivity vs. inverse temperature (N0bS: full circles and N0b: full squares); NMC cluster conductivity σ_{CS} (blue), NMC sample conductivity σ_{SS} (red); conductivity $\sigma_{sol/S}$ including PVdF/NMC interface (green). The black arrow is the freezing temperature of EC:DMC.

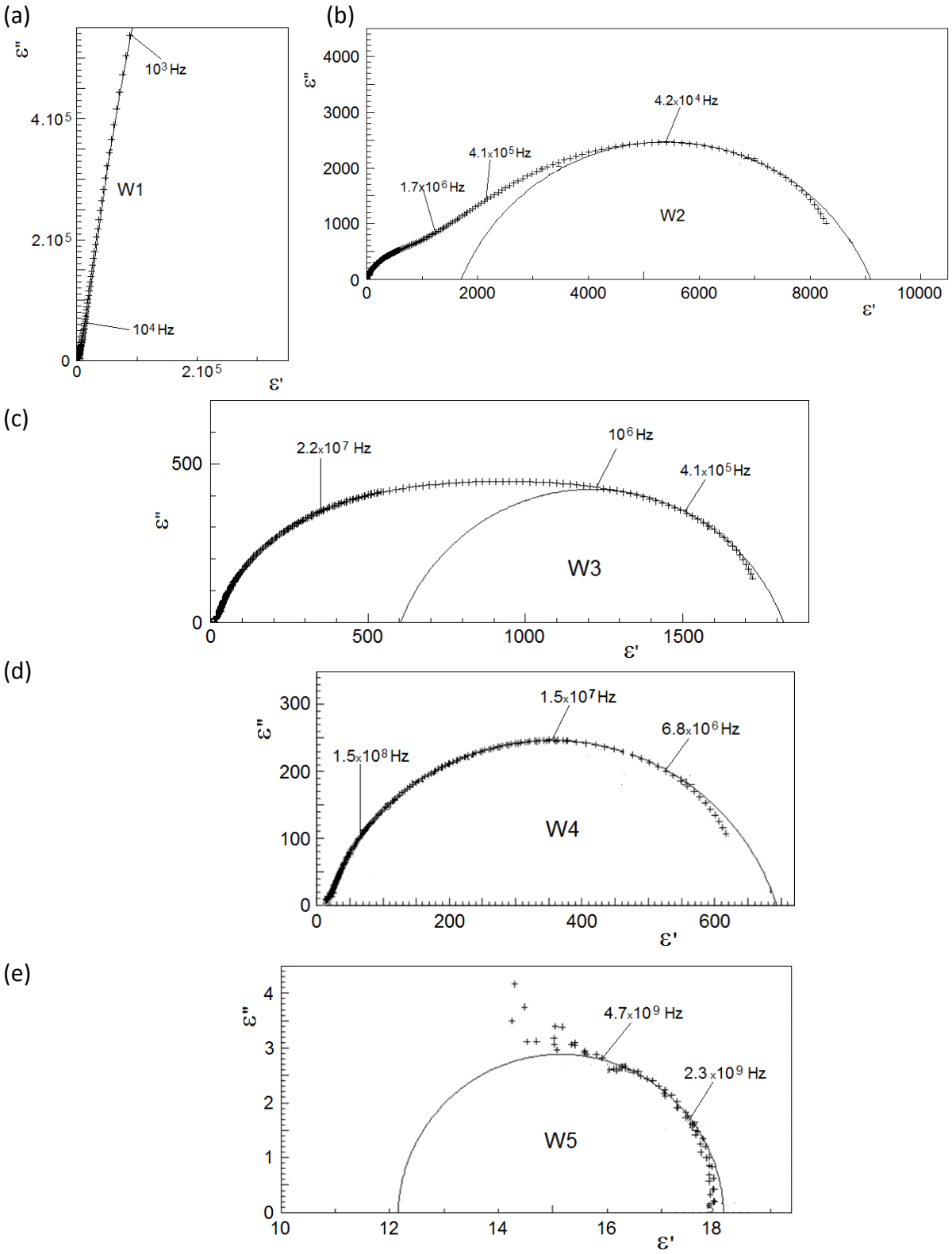

Fig. 8. a) Nyquist plots of complex permittivity, ε”(ω) vs. ε’(ω) of sample filled by LP30, i.e. N0bE (NMC532: 68.6 %; PVdF: 5%; LP30: 26.4 %) at 295 K. a) Low-frequency part of the plot: evidence of the giant dielectric relaxation domain W1 *(semi-circle)*. b) Plot obtained upon subtracting the contribution W1: evidence of the dielectric relaxation W2 *(circular arc)*. c) Plot obtained upon subtracting the contribution W2: evidence of the dielectric relaxation W3 *(circular arc)*. d) Plot obtained upon subtracting the contribution W3: evidence of the dielectric relaxation W4 *(circular arc)*. e) Plot obtained upon subtracting the contribution W4: evidence of the dielectric relaxation W5 *(circular arc)*. Electrolyte LP30: 1 M of LiPF6 EC:DMC 1:1.

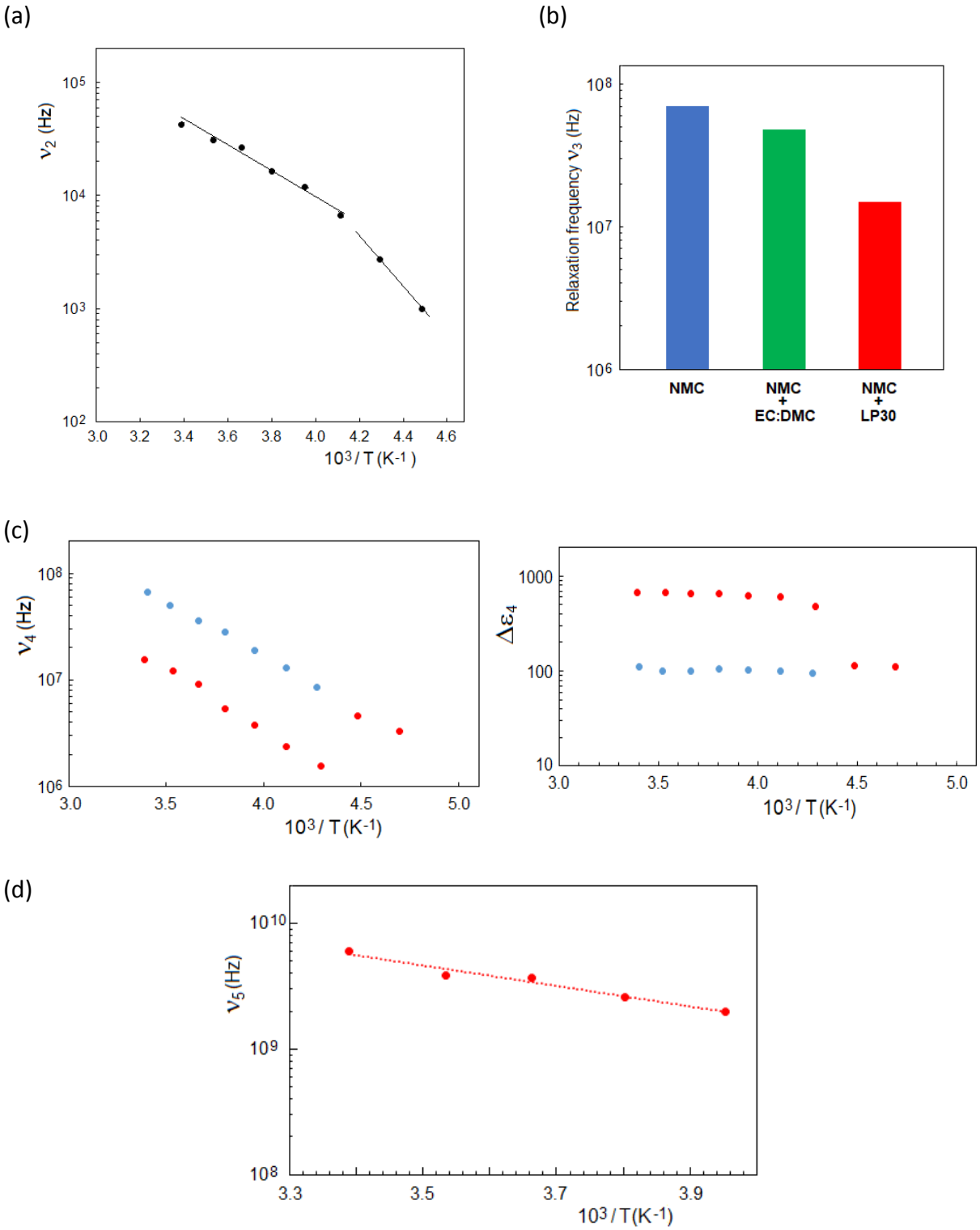

Fig. 9. (a) Relaxation frequency ν_2 of ionic motions in N0bE. (b) Comparisons of relaxation frequencies ν_4 of NMC cluster polarization at RT. (c) Temperature dependence of dielectric strengths $\Delta\varepsilon_4$ of NMC cluster polarization for sample N0bE filled by LP30 (•)and for dry sample N0b (•). (d) Relaxation frequency ν_5 of EC dipole rotation vs. inverse temperature.

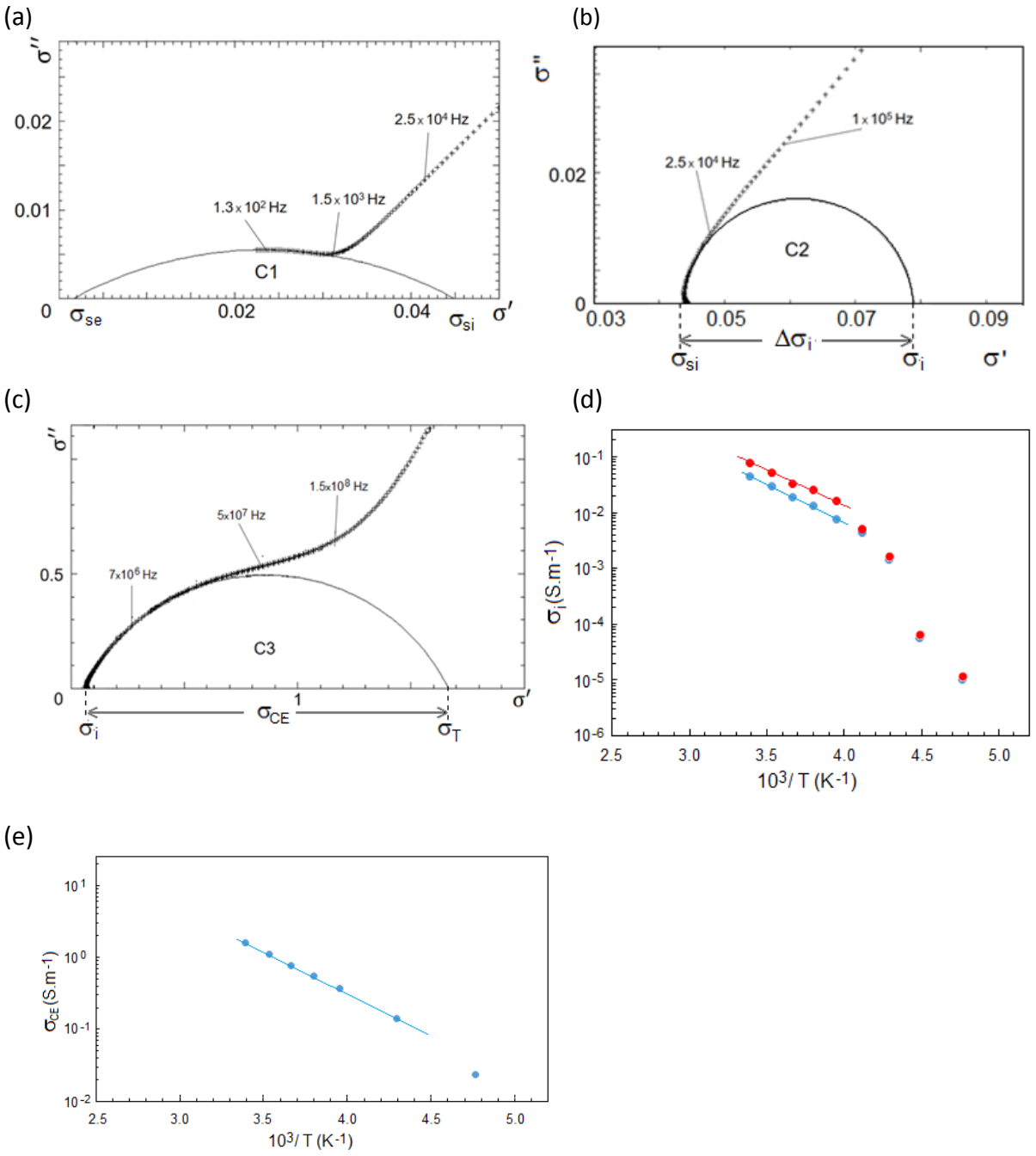

Fig. 10. Nyquist plots of the imaginary part σ”(ω) vs. the real part σ’(ω) of the complex conductivity of NMC532 filled by LP30 (N0bE) at 295 K: a) low frequency part of the spectrum and evidence of the relaxation domain C1 (arc of circle); b) plot obtained upon subtracting C1 and evidence of the relaxation domain C2 (arc of circle); c) plot obtained upon subtracting C2 and evidence of the relaxation domain C3 (arc of circle). σ_{si} = bulk ionic conductivity, σ_i = local (or diffusive) ionic conductivity, σ_{CE} = NMC532 cluster conductivity and $\sigma_T = \sigma_I + \sigma_{CE}$. Arrhenius plots of: d) ionic conductivities σ_{si} and σ_i, and e) NMC532 cluster (electronic) conductivity σ_{CE}.

(a)

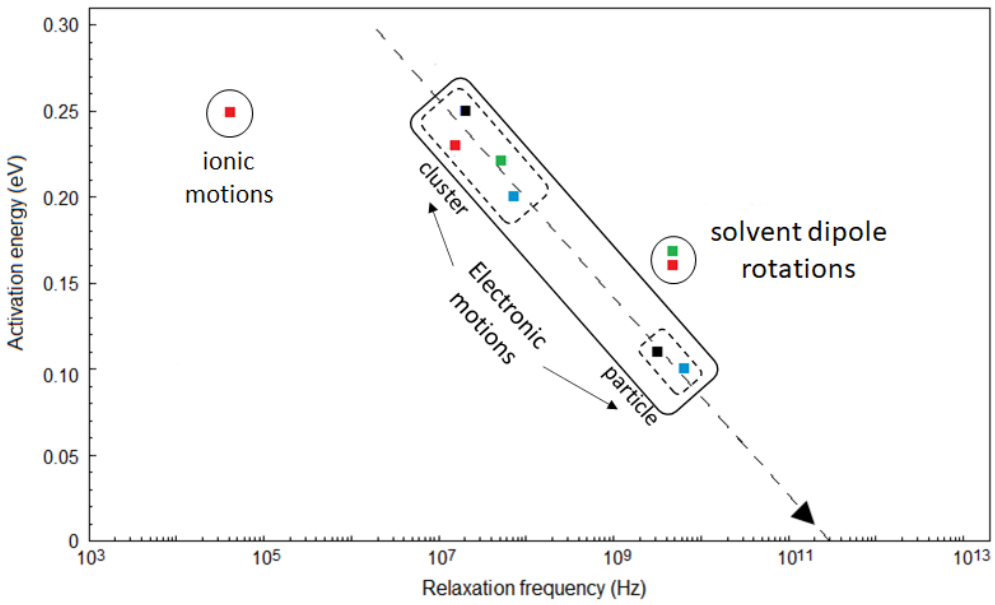

(b)

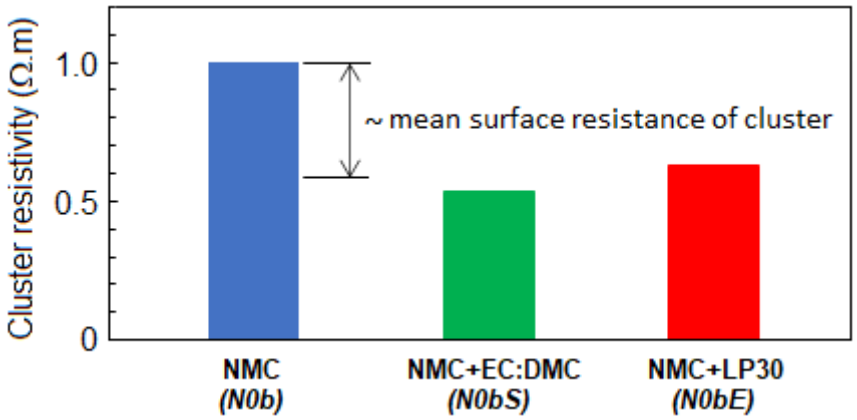

Fig. 11. a) Activation energies vs. relaxation frequencies at 295 K attributed to: ionic motions (Li^+, PF_6^-) in pore network filled with LP30, solvent dipole rotations (i.e. EC) and electronic motions (i.e., holes) in clusters and particles of NMC532 and NMC333. [5] The slope of the dotted line with an arrow is kT×ln10 with T ≈ 295 K and gives an average frequency prefactor around 3×10^{11} Hz (for electronic motions) at zero activation energy. Symbols used: dry NMC333 (■) [5], dry NMC532 *(N0 and N0b)* (■), NMC 532 filled with EC:DMC *(N0bS)* (■) and NMC 532 filled with LP30 *(N0bE)* (■). b) Influence of adsorbed solvent dipoles (EC in EC:DMC and LP30) and ions (PF_6^- in LP30) on total resistivity of NMC532 clusters. The drop of the total resistivity is proportional to the mean surface resistance of the cluster of the dry compound N0b.

FOR TABLE OF CONTENTS ONLY

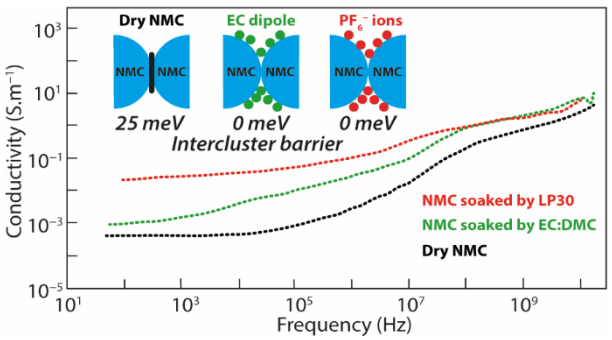

1015

REFERENCES

[1] Besnard, N.; Etiemble, A.; Douillard, T.; Dubrunfaut, O.; Tran-Van, P.; Gautier, L.; Franger, S.; Badot, J.-C.;. Maire, E.; Lestriez B. Multiscale morphological and electrical characterization of charge transport limitations to the power performance of positive electrode blends for lithium-ion batteries, *Adv. Energy Mater*, **2017**, *7*, 1602239.

[2] Badot, J.C.; Ligneel, E.; Dubrunfaut, O.; Guyomard, D.; Lestriez, B. A multiscale description of the electronic transport within the hierarchical architecture of a composite electrode for lithium batteries. *Adv. Funct. Mater.* **2009**, *19*, 2749-2758.

[3] Panabière, E.; Badot, J.C.: Dubrunfaut, O; Etiemble, A.; Lestriez, B. Electronic and Ionic Dynamics Coupled at Solid-Liquid Electrolyte Interfaces in Porous Nanocomposites of Carbon Black, Poly(vinylidene fluoride), and γ-Alumina. J. Phys. Chem. C, 121, 8364-8377 (2017).

[4] Seid, K.A.; Badot, J.C.; Dubrunfaut, O.; Caldes, M.T.; Stephant, N.; Gautier, L.; Guyomard, D.; Lestriez, B. Multiscale electronic transport in $Li_{(1+x)}Ni_{(1/3-u)}Co_{(1/3-v)}Mn_{(1/3-w)}O_2$: a broadband dielectric study from 40 Hz to 10 GHz. *Phys. Chem. Chem. Phys.* **2013**, *15*, 19790-19798.

[5] Seid, K.A.; Badot, J.C.; Perca, C; Dubrunfaut, O.; Soudan, P.; Guyomard, D.; Lestriez, B. An in situ multiscale study of ion and electron motion in a lithium-ion battery composite electrode. *Adv. Energy Mater.* **2015**, *5*, doi: 10.1002/aenm.201400903.

[6] Berthumeyrie, S.; Badot, J.C.; Pereira-Ramos, J.-P.; Dubrunfaut, O.; Bach, S.; Vermaut, Ph. Influence of the lithium insertion on the electronic transport in electroactive MoO_3 nanobelts and classical powders: morphological and particle size effects. *J. Phys. Chem. C* **2010**, *114*, 19803-19814.

[7] Belhadj-Tahar, N.-E.; Fourrier-Lamer, A. Broadband analysis of a coaxial discontinuity. *IEEE Trans. Microwave Theory Tech.* **1986**, *34*, 346-350.

[8] Kim, J., Lee, H., Cha, H., Yoon, M. & Park, M. Prospect and Reality of Ni-Rich Cathode for Commercialization, *Adv. Energy Mater.*, **2018**, *8*, 1702028.

[9] Tambio, S. J.; Cadiou, F.; Maire, E.; Besnard, N.; Deschamps, M.; Lestriez, B. The concept of effective porosity in the discharge rate performance of high-density positive electrodes for automotive application with the diffusion-limited penetration depth model, *J. Electrochem. Soc.*, **2020**, *167*, 160509

[10] Cadiou, F.; Douillard, T.; Besnard, N.; Lestriez, B.; Maire, E. Multi-scale characterization of the microstructure of composite electrodes for high energy density lithium ion batteries guided by the specificities of their electronic and ion transport mechanisms, *J. Electrochem. Soc.*, **2020**, *167*, 100521.

[11] Cadiou, F.; Douillard, Willot, F.; Badot, J.C.; Lestriez, B.; Maire, E. Effective electronic and ionic conductivities of dense EV-designed NMC-based positive electrodes by FFT numerical simulations on FIB/SEM volumes, *J. Electrochem. Soc.*, **2020**, *167*, 140504

[12] Meng, Y. S.; Ceder, G.; Grey, C. P.; Yoon, W.-S.; Jiang, M.; Bréger, J.; Shao-Horn, Y. Cation Ordering in Layered $O_3Li[Ni_x\ Li_{1/3-2x/3}\ Mn_{2/3-x/3}]O_2$ ($0 \leq x \leq 1/2$) Compounds. *Chem. Mater.* **2005**, *17* (9), 2386–2394.

[13] Jarvis, K. A.; Deng, Z.; Allard, L. F.; Manthiram, A.; Ferreira, P. J. Atomic Structure of a Lithium-Rich Layered Oxide Material for Lithium-Ion Batteries: Evidence of a Solid Solution. *Chem. Mater.* **2011**, *23* (16), 3614–3621.

[14] Madelung, O. *Introduction to Solid State Theory*; Springer Verlag, Berlin, **1981**.

[15] Kirkpatrick, S. Percolation and Conduction. *Rev. Mod. Phys.* **1973**, *45*, 574-588.

[16] Turban, L. On the effective-medium approximation for bond-percolation conductivity. *J. Phys. C: Solid State Phys.* **1978**, *11*, 449-459.

[17] Sato, N. *Electrochemistry at Metal and Semiconductor Electrodes*; Elsevier, Amsterdam, **1998**.

[18] Gerischer, H. *Advances in Electrochemistry and Electrochemical Engineering, Vol. 1*, Eds. Delahay P. and Tobias Ch. W., Interscience Publ., New York 1961.

[19] Xu, S.; Luo, G.; Jacobs, R.; Fang, S.; Mahanthappa, M.K.; Hamers, R.J.; Morgan, D. Ab Initio Modeling of Electrolyte Molecule Ethylene Carbonate Decomposition Reaction on $Li(Ni,Mn,Co)O_2$ Cathode Surface. *ACS Appl. Mater. Interfaces* **2017**, *9*, 20545-20553.

[20] Wohde, F.; Balabajew, M.; Roling, B. Li^+ Transference Numbers in Liquid Electrolytes Obtained by Very-Low-Frequency Impedance Spectroscopy at Variable Electrode Distances. *J. Electrochem. Soc.* **2016**, *163*, A714-A721.

[21] Debye, P. and Falkenhagen, H. Dispersion of conductivity and dielectric constant in strong electrolytes. *Phys. Z.* **1928**, *29*, 121, 401.

[22] Cadiou, F.; Douillard, T.; Willot, F.; Badot, J.C.; Lestriez, B.; Maire, E. Effective Electronic and Ionic Conductivities of Dense EV-Designed NMC-Based Positive Electrodes using Fourier Based Numerical Simulations on FIB/SEM Volumes. *J. Electrochem. Soc.* **2020**, *167*, 140504.

[23] Usseglio-Viretta, F. L. E., Colclasure, A.; Mistry, A.N.; Claver, K.P.Y.; Pouraghajan, F.; Finegan, D.P.; Heenan, T.M.M.; Abraham, D.; Mukherjee, P.P.; Wheeler, D.; Shearing, P.; Cooper, S.P., Smith, K. Resolving the discrepancy in tortuosity factor estimation for Li-ion battery electrodes through micro-macro modeling and experiment. *J. Electrochem. Soc.*, **2018**, *165*, A3403-A3426.

[24] Thorat, I.V.; Stephenson, D.E.; Zacharias, N.A.; Zaghib, K.; Harb, J.N.; Wheeler, D.R. Quantifying tortuosity in porous li-ion battery materials. *J. Power Sources*, **2009**, 188, 592-600.

[25] Zacharias, N.A.; Nevers, D.R.; Skelton, C.; Knackstedt, K.; Stephenson, D.E.; Wheeler, D.R. Direct Measurements of Effective Ionic Transport in Porous Li-Ion Electrodes. *J. Electrochem. Soc.* **2013**, *160*, A306-A311.

[26] Tambio, S.J. Evaluation of electrochemical performance of lithium-ion batteries and measurements of their transport properties by high-field NMR. *PhD Thesis*, Université de Nantes, **2019**.

[27] Landesfeind, J.; Gasteiger, H.A. Temperature and Concentration Dependence of the Ionic Transport Properties of Lithium-Ion Battery Electrolytes. *J. Electrochem. Soc.* **2019**, *166*, A3079-A3097.